THE ASTROPHYSICAL JOURNAL, 310:238–260, 1986 November 1

EVOLUTION AND INFRARED SPECTRA OF BROWN DWARFS

JONATHAN I. LUNINE, WILLIAM B. HUBBARD, AND MARK S. MARLEY
Lunar and Planetary Laboratory, University of Arizona, Tucson
Received 1986 January 15; accepted 1986 April 8

ABSTRACT

The recent detection of a subluminous companion to the M dwarf star VB 8 has renewed interest in the characteristics of self-luminous objects spanning the mass range from Jupiter to hydrogen-burning stars. We have constructed atmospheric and interior models of objects up to 0.05 $M_\odot$, to understand the relationship of "brown dwarfs" such as the VB 8 companion both to low-mass stars and to the well-studied Jovian planets. The atmospheric model solves the equation of radiative transfer in the gray atmosphere approximation by reducing frequency-dependent opacities due to H_2, He, H_2O, CO, and CH_4 to their Rosseland and Planck mean values. Condensation of iron and silicates occurs in some models, and the effect of such grains as opacity sources is assessed. The luminosity is due to degenerate cooling following a collapse phase and deuterium burning; a fully convective isentropic interior model is constructed using as an outer boundary condition the temperature and pressure level at which the atmosphere becomes convective. The interior model for brown dwarfs in the degenerate phase is analogous to that of Jupiter, with a large liquid metallic hydrogen core and a thinner molecular hydrogen envelope. The oxidation state of the atmosphere is a function of the object's mass: a 0.05 $M_\odot$ object 10^9 yr old has CO as the dominant carbon species rather than CH_4, as in the Jovian planets. As a result, the calculated infrared spectrum of such an object is extremely sensitive to the ratio of carbon to oxygen in the atmosphere. Using constraints on the radius provided by the interior models and the flux measured from V8 8B in the 1.6 and 2.3 μm regions of the spectrum, we conclude that VB 8B has an effective temperature between 1200 and 1500 K and that its atmosphere must be dominated by grains. The mass of VB 8B is constrained only as well as its age is; values in the range of 0.03–0.07 $M_\odot$ are plausible. We display the cooling curves of brown dwarfs of different masses and indicate changes in the chemical state of the atmosphere during the evolution which have dominant effects on the infrared spectrum. Such calculations suggest the possibility of deriving significant information on the age and composition of brown dwarfs from future infrared observations.

Subject headings: infrared: spectra — stars: evolution — stars: interiors — stars: late-type

I. INTRODUCTION

Brown dwarfs are self-gravitating, self-luminous objects which shine by virtue of the virialization of the gravitational energy of collapse accompanying formation and have insufficient mass to sustain hydrogen fusion reactions in their interiors. This class of object represents the continuation of the stellar main sequence to effective temperatures and luminosities below the so-called hydrogen-burning limit (see, e.g., Probst 1983) and has until recently remained entirely theoretical with the exception of the planets Jupiter and Saturn (which radiate more energy than they receive from the Sun; Hubbard 1980). The potential importance of such objects in resolving various missing mass problems in astrophysics (see § II) has sustained a modest level of interest in theoretical models and observational searches.

The recent discovery by McCarthy, Probst, and Low (1985, hereafter MPL) of a low-luminosity companion to the late M dwarf star VB 8 has renewed interest in the theoretical properties of this class of objects and opened the possibility of comparing detailed models with spectroscopic data to derive age, physical properties, and compositional information. At the same time, advances in our understanding of the properties of the Jovian planets and improvements in models for the behavior of hydrogen and helium at high pressure allow the possibility of constructing a continuum of models from stellar-mass objects to Jupiter. Predicted luminosities and spectral signatures based on these models will be of use in planning observational strategies for detecting objects in this mass range.

The present paper is a preliminary study of the physical and chemical nature of brown dwarfs which attempts to address the above issues. The outputs of the model are total luminosity and spectral distribution of emergent flux as a function of age, mass, and chemical composition. Properties of the interior and atmospheres of brown dwarfs are compared to those of the well-studied Jovian planets at one extreme of the mass spectrum, and with those of late-type main-sequence stars at the other. Physical and chemical properties of the VB 8 companion (VB 8B) are deduced from the modeling, but emphasis is placed on specifying what additional observations are required to best constrain these properties, since the available data do not as yet permit a unique interpretation. A broad approach is taken in summarizing key signatures in the emergent spectra of the age, mass, and chemical composition of brown dwarfs.

The paper is organized as follows. Section II provides a brief literature review of the astrophysical issues which have generated interest in brown dwarfs, efforts at detection, and earlier theoretical modeling. The observations of MPL are reviewed along with the relevant astrometric data of Harrington, Kallarakal, and Dahn (1983) to provide a critical assessment of what physical properties of VB 8B are established by the observations. Section III discusses the general theoretical behavior of brown dwarf evolution based on earlier studies, most notably that of Stevenson (1978), and lists the important assumptions entering into the present models. Section IV presents the scheme for calculating model atmosphere temperature-pressure profiles and the resulting boundary con-

ditions for the interior models. Interior structure is calculated in § V, and evolution curves for various masses are constructed. In § VI emergent spectra based on the models are shown, and comparison with the VB 8B observations are made to deduce the properties of that object. Section VII summarizes the results of the preceeding three sections by indicating key chemical and physical transitions during the cooling of brown dwarfs and the resulting observable emergent spectra. Finally, § VIII briefly discusses what can be learned from future observations and summarizes the broader relationship of the work to issues of stellar and planetary evolution and the behavior of cosmically abundant materials under high pressure.

II. BACKGROUND

Interest in the nature and detectability of brown dwarfs has its origins in a number of astrophysical issues: (1) the "missing mass" problems (solar neighborhood, Galactic disk, and massive Galactic halos); (2) physics of stellar interiors, including hydrogen-burning mass limits and degenerate cooling; and (3) mechanisms of star formation and relationship to the formation of planets (Probst 1983). A series of papers, most recently those of Bahcall (1984), have concluded, based on dynamical arguments, that the ratio of total to observed matter in the solar neighborhood is at least 1.5. One possible interpretation is that the excess is present as faint M dwarf and cooler objects which have hitherto not been observed. The so-called luminosity function, which is a measure of the number of observed stars within a given absolute magnitude range (Mihalas 1968, p. 63), decreases with increasing magnitude for very late type M dwarfs; that this is due to observational effects is consistent with but by no means required by the dynamical arguments (see, however, Probst 1983; Reid and Gilmore 1984). Salpeter's initial mass function (Salpeter 1955), which gives stellar formation rate as a function of mass, has been interpreted as implying that the total mass of stars is dominated by objects below the hydrogen-burning limit of 0.08 $M_\odot$ (Stevenson 1978). (1 $M_\odot = 2 \times 10^{33}$ g.) Predicting the luminosity of such objects as a function of age has a direct bearing on their detectability and hence on testing the proposed solution to the missing mass problem.

Early theories of formation of the Jovian planets largely tend to emulate the Hayashi phase of stellar formation by modeling contraction of an adiabatic nonrotating body (Grossman *et al.* 1972; see Stevenson 1982*a* for a more extensive review). The initial phase of collapse is envisioned to involve fragmentation from a gaseous nebula (Cameron 1978). Such stellar-like origins suffer in not predicting the similarity in mass of dense cores inferred to be present in all four giant planets (Hubbard and MacFarlane 1980; Stevenson 1982*b*). A qualitatively different scenario, the "nucleated collapse," postulates accretion of rock and ice material to form a core, followed by hydrodynamic collapse of gas surrounding the core (Mizuno 1980). This model has had some success in predicting planetary core sizes. The possible existence of bound stellar systems containing brown dwarfs more massive than Jupiter raises the issue of where to apply the two qualitatively different formation scenarios; in § VIII we address whether compositional and other information derived from spectra of brown dwarfs, calculated in this paper, can help answer this question.

Theoretical models of brown dwarf physical properties have their origin in stellar and planetary structure and evolution studies. Literature on modeling of giant planet structures is reviewed in Hubbard and Stevenson (1984). The largest uncertainty is in understanding the complex thermodynamic behavior of the materials believed present in these bodies. Discussion of the assumptions going into such models is deferred to later sections, since our interior models have their origin in such efforts.

Literature on modeling of stellar structure and evolution is voluminous. Of most interest here is work on low-mass, late-type main-sequence stars and efforts to find the hydrogen-burning mass limit. Copeland, Jensen, and Jorgensen (1970) and VandenBerg *et al.* (1983) calculate the structure and evolution of main-sequence stars down to 0.1 $M_\odot$, considering carefully possible variations in heavy-element abundance. The latter paper improves over the former by treating in detail molecular opacities important to the atmospheric model. Determinations of the lower mass limits to hydrogen and deuterium burning were made in a series of papers by Graboske, Grossman, and colleagues (see, e.g., Graboske *et al.* 1975; Grossman, Hays, and Graboske 1974; Grossman and Graboske 1973), who modeled the early phases of evolution of objects from 0.5 to 0.001 $M_\odot$. Tarter (1975) extrapolated the results of the Grossman and Graboske work to derive cooling times in the degenerate stage for objects below the hydrogen-burning mass limit and predicted such objects would decrease sharply in luminosity after roughly 3×10^9 yr due to crystallization of their interiors and resulting Debye cooling. We argue below that Debye cooling is not relevant. D'Antona and Mazzitelli (1985), on the other hand, predict that objects just at the hydrogen-burning limit could take upward of 10^{10} yr to reach the main sequence. Finally, Nelson, Rappaport, and Joss (1985) used a simple polytropic interior model and a range of atmospheric opacities to calculate cooling curves for objects in the mass range 0.01–0.1 $M_\odot$. They conclude that the VB 8 companion is in excess of 0.04 $M_\odot$.

The most important theoretical study of brown dwarfs to date is that of Stevenson (1978). Using analytic representations of atmospheric opacity from Graboske *et al.* (1975) and the zero-temperature hydrogen-helium mass-radius relationship of Zapolsky and Salpeter (1969), an analytic expression for the degenerate cooling phase was derived. Very similar in approach is the work of Hubbard (1977), which is restricted to a 0.001 $M_\odot$ object.

Until recently, searches for brown dwarfs have relied on astrometric studies and infrared photometric searches. The former technique and a compilation of astrometric binaries as of 1978 are presented by Lippincott (1978). An observational bias in detecting low-mass companions favors low-mass primaries, and hence stars with very low luminosities. As a consequence, the determination of the companion mass involves an ambiguity depending on how much of the luminosity of the system is contributed by the companion. Photographic measurement of the separation has resolved this ambiguity in the case of the Ross 614 system (Probst 1977), which yields a companion mass of 0.07 $M_\odot$, just below the hydrogen-burning limit and the smallest yet determined. Infrared photometry has been employed in searches for isolated low-luminosity objects, direct observation of cool stars which could be candidate brown dwarfs (Probst and Liebert 1983), and detection of infrared excesses in white dwarf spectra which are ascribed to low-luminosity companions. Probst (1983) concludes from a survey using this last technique that there is a real flattening of the luminosity function beyond late M dwarfs. However, this approach cannot be used to detect companions around main-

sequence stars, because of either the very high luminosity of early main sequence primaries or the similarity in spectral energy distribution of a subluminous companion to that of its late main sequence primary. This technique has been used successfully with *IRAS* data to detect a number of dust disks around main-sequence stars (Aumann *et al.* 1984). Photometry of isolated objects has yielded one low-temperature object, with an anomalous infrared spectrum, which is either a candidate brown dwarf or a very cool hydrogen-burning main-sequence object (Probst and Liebert 1983). No detection of isolated or bound objects clearly below the hydrogen-burning mass limit has been reported from *IRAS* data.

Application of infrared speckle interferometry by MPL to observation of the late M dwarf VB 8 has resulted in detection and quantitative measurement of the flux from a low-luminosity companion in both H and K infrared bands. The technique and current results are reported in McCarthy (1986). Speckle interferometry of a similar spectral class star, VB 10, yields no detectable companion. MPL derive the following from their data plus the known distance to the system: blackbody temperature 1360 ± 200 K; luminosity $3 \times 10^{-5}\ L_\odot$; blackbody radius 0.09 $R_\odot$ ($1\ R_\odot = 7 \times 10^{10}$ cm). Using the inferred luminosity, estimated age of the system (of order 10^9 yr), and degenerate cooling curves of Stevenson (1978), they estimate a mass range of 0.03–0.08 $M_\odot$. How well the mass is determined hinges on the validity of (1) the degenerate cooling curve, (2) the assumed age of the system, and (3) the assumption that the object is a blackbody in deriving the luminosity from the broad-band fluxes. Since a radius is also derived along with the luminosity, consistency among mass, radius, and luminosity can be checked by constructing models of the object. Given a model radius, emergent spectra can be calculated to determine the effective temperature for different assumed compositions. We conclude, based on the modeling reported in this work, that the VB 8B effective temperature and luminosity derived by MPL from their photometry are internally consistent and physically reasonable for certain compositions. Also, the radius is sufficiently well constrained that the only free parameter remaining in determining the mass is the system age.

Harrington, Kallarakal, and Dahn (1983) reported detection of an astrometric companion to VB 8. The best estimate for the companion's mass, given the small arc of the orbit which has been observed, is $M \gtrsim 0.02\ M_\odot$ (Harrington 1986). Until more of the orbit is observed, little more regarding VB 8B can be gleaned from astrometry.

III. PHYSICAL PROCESSES IN BROWN DWARFS AND MODEL ASSUMPTIONS

For the purposes of this paper, we define a brown dwarf to be an electron-degenerate self-gravitating object, of solar or near-solar bulk composition, with interior temperatures below the range required for significant hydrogen fusion reactions, and with a mass in a range which covers about two orders of magnitude—from 2×10^{30} g (Jupiter) to 170×10^{30} g (0.085 $M_\odot$). The self-luminosity of a brown dwarf is derived primarily from a slow decline of interior temperature. This decline is accompanied by very modest changes in radius and interior density profile, as is assured by the electron degeneracy. The cooling of brown dwarfs is thus analogous to the late evolution of white dwarfs, but because of the much lower electron densities in brown dwarf interiors, thermal effects in the equation of state are significant despite strong electron degeneracy.

Objects in the brown dwarf mass range have interior equations of state in which electrostatic interactions between the pressure-ionized electrons and protons play a major role. The interactions steepen the pressure-density relation, so that the effective polytropic index is modified from the value of 1.5, which would obtain for noninteracting, nonrelativistic electrons and protons. At the lower end of the brown dwarf mass range, the effective polytropic index is closer to 1.0. As discussed by Zapolsky and Salpeter (1969), there is consequently a maximum radius for zero-temperature objects of solar composition; this maximum radius is $\sim$70,000 km and is achieved by objects about twice the mass of Jupiter. All the models considered in this study have similar radii, generally within 25%–30% of 70,000 km. Thermal effects are quite significant in our models, however, and it would not be an adequate approximation to use the zero-temperature models of Zapolsky and Salpeter to describe their interior structure. Polytropes of index 1.5 are likewise a somewhat crude approximation to the structure of our brown dwarf models, particularly in the lower mass range.

Three stages are identified in the evolution of brown dwarfs with masses greater than 0.01 $M_\odot$ (Grossman and Graboske 1973; Stevenson 1978): a hydrodynamic collapse phase of roughly constant effective temperature (but decreasing radius); a phase of deuterium fusion; and degenerate cooling, in which the virialized energy of gravitational collapse is released and is characterized by decreasing effective temperature and slowly declining radius. The first two stages are over in $\sim 2 \times 10^8$ yr; for objects less than $\sim$0.01 $M_\odot$, deuterium burning does not occur, and the onset of degenerate cooling occurs sooner. A fourth and final stage may also be identified, in which interior temperatures become sufficiently low that major constituents, such as helium and eventually hydrogen, begin to condense out, prolonging the cooling process. Stevenson and Salpeter (1977*b*) have proposed that helium is condensing in Saturn, although the thermodynamic description of liquid metallic hydrogen-helium mixtures used in the present study does not predict such a transition at a high enough temperature for it to be significant in Jupiter or Saturn. Neither theory would predict the onset of the fourth phase for models considered in the present study.

The present study focuses on the third stage of evolution, as this is where the major part of the lifetime of a brown dwarf is spent (Stevenson 1978). We exclude hydrogen fusion reactions and other sources of luminosity, such as incident radiation or matter from a bound companion star (important for the evolution of Jupiter and Saturn), and mass outflow or inflow involving the object. This study concentrates on objects in the mass range from 0.015 to 0.050 $M_\odot$ and effective temperatures in the range $1000 \lesssim T_e \lesssim 2000$ K, which are most likely to be representative of extrasolar brown dwarfs which could be observable in the forseeable future. This study could be extended using the same general approach to encompass the evolution of Jupiter- and Saturn-mass objects, although some modifications of the model atmosphere grid calculations would be necessary. Such a study will be carried out in the near future.

The modelling strategy begins by constructing atmospheric temperature-pressure structures for specified compositions and surface gravities for a range of effective temperatures. These models are analyzed to assess consistency of the temperature structure with the assumed abundance of various molecular species and cloud condensates. The models are then adjusted if required. The approximate temperature and pressure at which

the deep convection zone begins is used as the boundary condition to the interior model, which produces a self-consistent temperature-pressure-density structure that determines the radius (and hence mass) of the object. A sequence in effective temperature of such objects at a fixed mass then constitutes an evolutionary track. Finally, the atmospheric models are used to generate emergent spectra which are characteristic of the effective temperature and composition of the object.

For convenience we outline the major assumptions of the calculation below:

1. Composition.—We assume the objects have a solar proportion of hydrogen to helium, and that these materials dominate the composition. The abundance of Z-elements is variable; a baseline model involves solar proportions, but in particular the C to O ratio is varied in some models. The possibility of a strong enhancement of heavy elements, in nonsolar proportions, in the envelope of Jupiter (Bjoraker 1985; Hubbard 1986) compels us to consider such variations. Solar abundances are from Anders and Ebihara (1982).

2. Atmosphere.—The outer envelope or "atmosphere" is here defined as that region in which the ideal gas equation of state for H_2–He is a valid approximation. This sets the bottom boundary of the atmosphere at $T \approx 2500$ K; for temperatures above this, the contribution of dissociated hydrogen becomes important in determining the adiabatic temperature gradient. In practice, the atmospheric calculations are terminated at the top of the deep convective zone (see "3. Interior," below).

The atmosphere is assumed to be plane parallel and isotropic, the former justified by the small density scale height relative to the total radius in the region of interest. Hydrostatic equilibrium is assumed to apply. This excludes objects undergoing hydrodynamic collapse. The effects of radiation pressure and turbulent stresses on the equation of hydrostatic equilibrium are small for the masses and luminosities considered in this study.

We assume the atmosphere to be in local thermodynamic equilibrium (LTE), that is, processes involving primarily scattering of radiation as opposed to absorption and reemission are excluded. This assumption is generally a good one for the pressure-temperature regime and frequency interval (1–10 μm) relevant to this study, since fine structure in the line spectra of molecular species is substantially pressure-broadened. At some frequencies, radiation is emitted at altitudes much higher than that from which the bulk of the thermalized emission occurs, and we cannot exclude non–LTE processes in line radiation here. The importance of Rayleigh scattering in some models also violates this assumption and is treated only approximately here. Finally, the presence of condensates in some models raises the possibility that scattering processes could play an important role in the radiative transfer; however, the cloud compositions considered make it likely that true absorption processes will dominate scattering.

Finally, we assume the gray atmosphere approximation to the equation of radiative transfer and use suitably frequency-averaged opacities in solving for the temperature-pressure structure of the atmosphere. The justifications for such an approach lie in the approximate nature of the outputs desired from the model and the robustness of the conclusions based on such calculations.

3. Interior.—Like the atmosphere, the interior is assumed to be in hydrostatic equilibrium, with no significant changes over times short compared with the Kelvin time. The interior is assumed to be fully convective, chemically homogeneous, and isentropic from the base of the atmosphere to the center. Thus the temperature structure throughout the interior is smoothly adiabatic. The assumptions of convective transport and adiabaticity have been extensively justified for Jupiter in the literature; reviews are given by Stevenson and Salpeter (1976) and Hubbard and Smoluchowski (1973). These arguments apply even more strongly to the more massive and luminous degenerate objects considered here. Radiative heat transport is neglected because thermal photons cannot propagate in the interior, owing to the high electron density. Thermal conduction by electrons in metallic hydrogen is evaluated using an expression given by Stevenson and Salpeter (1977*a*); we note that this expression has the same density dependence as an earlier formula given by Hubbard and Lampe (1969) but with a coefficient about a factor of 2 larger. All our models are verified to be convectively unstable essentially throughout their interiors and evolutionary lifetimes, although the most massive models considered here (0.05 $M_\odot$) do develop small ($\sim 10\%$ of toal mass) conductive cores near the end of their evolutionary tracks at an age of 5.5×10^9 yr. In general, convection in the liquid metallic hydrogen interior is highly efficient, keeping temperature gradients very close to the adiabatic temperature gradient. The arguments leading to these conclusions break down for rapidly rotating objects or for objects with strong magnetic fields, which we exclude from consideration here.

The assumption of complete isentropy, from the base of the atmosphere to the center, is thus an essential feature of our models. However, uncertainties in the hydrogen phase diagram are such that we are not assured that this is valid. Current indications are that there is a transition from the molecular state of hydrogen to the metallic state at a pressure of ~ 3 Mbar (Stevenson and Salpeter 1976; Nellis *et al.* 1983). In Jovian models this pressure is at a temperature of ~ 7000 K, while in higher mass brown dwarf models it is at temperatures of 10,000–30,000 K. We do not known whether the liquid-liquid transition from molecular hydrogen (H_2) to metallic hydrogen (H^+) is a first-order thermodynamic transition involving an entropy discontinuity at constant temperature and pressure. If it is, then the interior adiabat could be "mismatched" to the atmospheric adiabat by as much as some tens of percent in the corresponding temperature profile, with a sign depending on the sign of the entropy jump. Moreover, if there *is* a first-order $H_2 \rightarrow H^+$ transition between liquid phases, it must terminate in a critical point at some temperature. Conceivably a brown dwarf interior adiabat could initially pass above this critical point and, with subsequent cooling, eventually intersect it.

The $H_2 \rightarrow H^+$ transition occurs in the outermost layers of the brown dwarf models (layers which enclose $>99\%$ of the mass for all models considered in this paper), and thus its effects could be included in the description of the atmospheric surface condition. We do not explicitly model a possible first-order transition in this paper because of the difficulty of reliably calculating the sign or value of the latent heat (if any). However, we estimate that this uncertainty will not substantially exceed other uncertainties (exhibited in § IV) in the atmospheric surface conditions and in the matching of surface and interior adiabats.

Finally, the assumption of chemical homogeneity may be questionable, particularly in the lowest mass objects considered here. It is by now well known that the interior of Jupiter is substantially enriched in elements other than hydrogen and helium, relative to solar composition, and that both

Jupiter and Saturn possess dense cores. The most recent analysis (Hubbard 1986) finds that there may be a substantial gradient in such dense material even within the predominantly metallic hydrogen envelope, as suggested by Stevenson (1985). The origin of Jovian-class objects appears to involve processes of selective accretion and escape of volatiles which may lead to a zoned structure, with concomitant repercussions on the assumptions of complete isentropy. Even the more massive objects modeled here could be subject to such complications, although this is not considered in the present calculations.

IV. DETERMINATION OF ATMOSPHERIC TEMPERATURE-PRESSURE STRUCTURE

a) Formalism

Consider a plane-parallel atmosphere in local thermodynamic and radiative equilibrium. If the opacity κ (here expressed as mass absorption coefficient) is frequency-independent, or an appropriate choice of frequency-independent opacity can be made, the solution to the equation of radiative transfer is

$$T(P)^4 = \tfrac{3}{4}T_e^4[\tau + q(\tau)] \tag{1}$$

(Chandrasekhar 1960, p. 294), where $T(P)$ is temperature at pressure level P, T_e is the effective temperature (defined below), and τ is the optical depth defined on a pressure scale so that $d\tau = \kappa dP/g$, where g is the gravitational acceleration. We use the Eddington approximation to assign $q(\tau) = \frac{2}{3}$; Mihalas (1978, p. 62) notes that this produces errors in the mean flux of less than 16%. For a particular choice of frequency-averaged opacity κ, equation (1) specifies the temperature-pressure structure for an atmosphere in radiative equilibrium. The emergent flux F_ν as a function of wavenumber can then be computed:

$$F_\nu = 2\int_0^\infty B(\nu, T)E_2(\tau' - \tau)d\tau' , \tag{2}$$

where the Planck function $B(\nu, T)$ is

$$B(\nu, T) = 2h\nu^3 c\,\frac{1}{\exp(h\nu c/kT) - 1} ; \tag{3}$$

here h is Planck's constant, c is the speed of light, and ν is the wavenumber. The second exponential integral over all emission angles π to $-\pi$ is calculated as a function of the frequency-dependent optical depth $\kappa dP/g$, using polynomial representations from Abramowitz and Stegun (1968, p. 231). Quantities subscripted with ν are frequency-dependent. The effective temperature is then given by

$$T_e^4 = \frac{\pi}{\sigma}\int_0^\infty F_\nu d\nu , \tag{4}$$

where σ is the Stephan-Boltzmann constant.

In general, the effective temperature calculated in equation (4) will not equal that used in equation (1), because the temperature profile was derived using a gray opacity while the emergent flux was calculated from the fully frequency-dependent values. What we require, then, are two opacity averaging schemes which produce temperature profiles that bracket the "true" profile which actually satisfies the constraint of radiative equilibrium, that is, for which T_e in equation (4) equals that in equation (1). Based on Mihalas (1978, p. 56), we use the Planck κ_P and Rosseland κ_R mean opacities:

$$\kappa_P = \frac{\int_0^\infty \kappa_\nu B(\nu, T)d\nu}{\int_0^\infty B(\nu, T)d\nu} , \tag{5}$$

$$\kappa_R^{-1} = \frac{\int_0^\infty \kappa_\nu^{-1}\partial B(\nu, T)/\partial T d\nu}{\int_0^\infty \partial B(\nu, T)/\partial T d\nu} . \tag{6}$$

The Planck mean weights most highly the largest opacities and hence produces high temperatures for a particular set of κ_ν; we find that T_e(eq. [4]) > T_e(eq. [1]). The Rosseland mean weights the smallest opacities most highly; it produces low temperatures for a given set of opacities and, except for pathological cases, T_e(eq. [4]) < T_e(eq. [1]). We therefore argue that the true temperature profile lies between the profiles which use gray opacities calculated from equations (5) and (6). Calculation of the Rosseland and Planck mean opacities also allows an estimation of the boundary temperature T_0 obtained as optical depth goes to zero:

$$T_0 = T_e\left(\frac{1}{4}\frac{\kappa_R}{\kappa_P}\right)^{1/8} \tag{7}$$

(Mihalas 1978, p. 212). For a frequency-independent opacity, equation (7) goes to the appropriate gray atmosphere limit.

The imposition of radiative equilibrium on an atmosphere in which the opacity increases with increasing pressure must at some point produce a temperature gradient dT/dP which exceeds the so-called adiabatic temperature gradient $dT/dP|_{ad}$. The atmosphere is then considered to be in convective equilibrium (Mihalas 1978, p. 186), with a temperature gradient which to a very high degree of accuracy is given by the adiabatic value

$$\left.dT/dP\right|_{ad} = \frac{R}{C_p}\frac{T}{P} \tag{8}$$

for an ideal gas (Reif 1965, p. 159). For a solar H_2-He mixture, C_p/R (the molar specific heat at constant pressure divided by the gas constant) is 3.3 (Weast 1967, p. D-96); at the temperatures of interest for observable extrasolar brown dwarfs ($T_e \gtrsim 1000$ K), this value is insensitive to the para- to ortho-hydrogen ratio (Conrath and Gierasch 1983). As temperatures increase beyond 2000 K, the dissociation of H_2 produces a latent heat effect which substantially lowers the adiabat (Hayashi and Nakano 1963).

The formalism described above is used to compute the pressure level at which the "deep" convection zone begins and to construct emergent spectra for various choices of surface gravity, effective temperature, and composition. The term "deep" is used to distinguish the adiabatic region which forms a continuous zone with the deep interior from convective regions restricted in extent and caused by sharp opacity variations in the atmosphere (due, e.g., to cloud formation). We discuss in § V the sensitivity of the model structures and evolution to our choice of pressure and temperature at the top of the convection zone. We do not attempt to calculate a fully consistent radiative-convective temperature profile in constructing these spectra; instead we use the radiative profile. The effect of this approximation is discussed in § VI.

Figure 1 plots temperature profiles in a 0.05 $M_\odot$, 0.1 $R_\odot$ object with an effective temperature of 1500 K, for Planck mean and Rosseland mean opacities. The source of opacity is

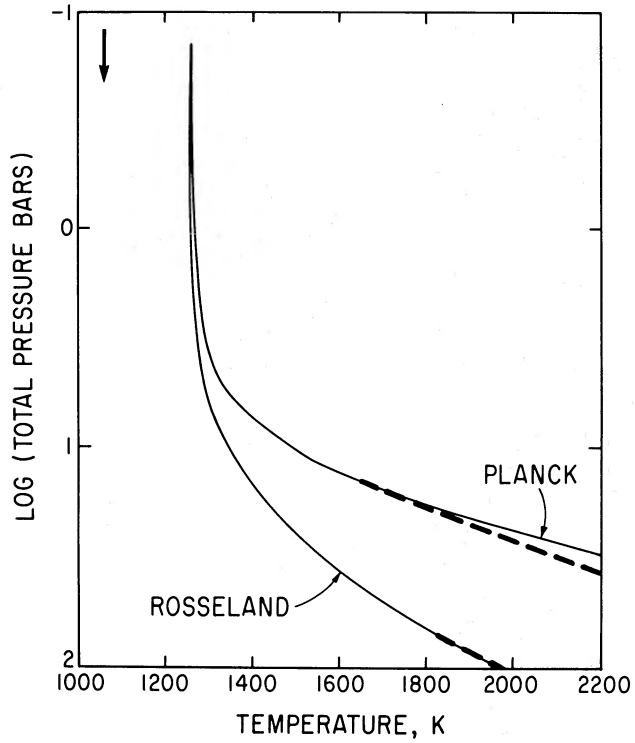

FIG. 1.—Temperature profile in a brown dwarf atmosphere containing hydrogen and helium as the sole sources of opacity, for an effective temperature of 1500 K, 0.05 $M_\odot$, and 0.1 $R_\odot$. Arrow indicates nongray skin temperature estimate. Labels refer to choice of opacity averaging scheme (see text).

pressure-induced hydrogen-helium absorption as well as H^- and H_2^- transitions at higher temperatures (the treatment of these sources is discussed in § IV*b*). The onset of convection is indicated for the Planck mean; the Rosseland mean profile is very close to a convective profile (but still radiative) down to a level at which hydrogen dissociation begins to lower substantially the adiabatic gradient (above 2500 K). The nongray correction to the skin temperature (optical depths much less than unity) from equation (7) is shown by an arrow. In § V we assess the sensitivity of the structure and evolution models to the differing temperature profiles, and we examine the appearance of the emergent flux in § VI.

b) Sources of Opacity

We divide the opacity sources considered into three groups: hydrogen-helium (including pressure-induced H_2-He opacity, H^- and H_2^- opacities, and Rayleigh scattering); Z-component molecular sources H_2O, CO, CH_4, N_2, NH_3, and TiO; and opacity from condensed phases.

i) *Hydrogen and Helium*

The most important overall source of opacity for determining the basic atmospheric structure is pressure-induced absorption by molecular hydrogen. For objects with effective temperature less than 600 K, the translational and rotational transitions which occur below 2000 cm^{-1} are most important in determining the opacity, and the theoretical determinations of Trafton (1966) for pure hydrogen, along with enhancement factors for a solar-abundance mix with helium in Linsky (1969) are used to calculate the absorption coefficient. The resulting temperature profile for Jupiter (T_e = 125 K) agrees fairly well with that of Hunten, Tomasko, and Wallace (1980), who used later formulations for H_2-He of Birnbaum and Cohen (1976), based on laboratory data.

Above an effective temperature of 600 K, the vibrational transitions above 3000 cm^{-1} begin to dominate. We use the calculated absorption coefficients of Patch (1971) and Linsky (1969) with corrections for the presence of helium based on integrated absorption coefficients in Linsky (1969). Patch criticized the Linsky work because the latter used a simple Lennard-Jones interaction potential between H_2 molecules. The ratio of absorption coefficients at a particular frequency from the two studies ranges from 1 at low wavenumbers to 10 at 10^4 cm^{-1}, with the Patch coefficients being higher. The effect on the temperature profile is generally less than a factor of 2 in pressure at a given temperature; we use coefficients intermediate between those of Patch and Linsky. We do not reproduce the expressions for κ from the two papers here; it is sufficient to bear in mind that at a fixed frequency, the optical depth τ_{pi} due to pressure-induced absorption goes as

$$\tau_{pi}(P, T) = A(P, T)P^2/T , \quad (9)$$

where the pressure dependence is dominated by the P^2 factor.

At temperatures in excess of 2000 K in a solar composition gas, H^- and H_2^- become important sources of opacity, for two reasons: (1) at increased temperatures, equilibrium between hydrogen species and metals favors increasing mixing ratios of H^- and other ions; and (2) the peak of the Planck function is shifted to above 4000 cm^{-1}, where the pressure-induced molecular hydrogen opacity begins to fall rapidly. This latter effect is well illustrated in Figure 8 of Linsky (1969), in which opacity contributions due to neutral molecules and ions are superposed on a plot of opacity versus wavenumber for several (P, T) conditions. Even our models with effective temperatures of 1000 K are strongly affected by the high wavenumber opacity sources, since at deeper levels in the atmosphere the Planck function peaks at higher wavenumbers, and pressure-induced opacity becomes less important in determining the overall temperature even as pressure increases. Models run on a Rosseland mean temperature scale, for which lower opacities are weighted most highly, are particularly dominated by this shift in primary opacity source.

We use the polynomial fits tabulated in Gingerich (1964) and Mihalas (1967) for H^- bound-free and free-free absorptions, and H_2^- free-free absorptions, along with electron pressure in a solar composition atmosphere from Vardya (1965). The resulting dependence of absorption coefficient on wavenumber is essentially that of Linsky's Figure 8 (with the somewhat higher contribution from pressure-induced absorption as discussed above).

Finally, we include Rayleigh scattering in an approximate way, based on plots in Linsky (1969), by assuming the opacity resulting from the scattering to be true absorption. This is not, of course, correct, but Rayleigh scattering is the dominant opacity only over a rather narrow range of temperatures which are high enough to put the Planck peak at wavenumbers for which pressure-induced opacity is decreasing, but low enough that the hydrogen ion sources are not yet important. If the envelope is metal-poor and hence deficient in H^- and H_2^- opacity, Rayleigh scattering dominates shortward of 1 μm wavelength. We do not model this case here. We therefore treat the Rayleigh scattering as true absorption, which allows us to maintain the simple formalism outlined above.

ii) *Gaseous Molecular Line Opacity*

We consider gaseous species H_2O, CO, CH_4, and TiO. The first three molecules are expected to be the most abundant carbon and oxygen species in the pressure-temperature-composition regime considered; TiO, although much less abundant, is important at high wavenumbers, where the others are not spectroscopically active. The abundant molecule N_2 contributes only pressure-induced absorption which, because it is 10^4 times less abundant than H_2 in the gas, provides negligible opacity. NH_3 is not abundant under the (P, T) conditions encountered in brown dwarfs more massive and luminous than Jupiter; in Jupiter itself, it plays only a negligible role in determining the temperature structure (Hunten, Tomasko, and Wallace 1980). The above statements must be justified by imposing the condition of thermodynamic equilibrium on the gas for a given calculated (T, P) profile to determine whether the assumed composition of opacity sources is consistent. We do this in § IV*d*.

The highly nongray nature of the line spectra produced by the molecular species considered renders our approach using averaged opacities suspect, since the resulting Rosseland and Planck mean opacities differ greatly when the line spectra are included. These extreme temperature profiles tend, however, to fall between those of the pure hydrogen-helium case and those including grain condensates for most effective temperatures of interest. We show in § V that our evolution tracks are not greatly different for these two compositions, and hence treating the effects of molecules on the temperature profile is not a critical exercise. We are interested, however, in the effect of molecular line transitions on the broad-band emergent spectra computed from the models.

To incorporate molecular transitions we use a form of the Elsasser band model described by Edwards *et al.* (1967). This model assumes that the band is composed of regularly spaced pressure-broadened lines to produce an absorption coefficient of the form

$$\kappa_\nu = \frac{C_1}{C_3} \exp\left(-\frac{|\nu - \nu_0|}{C_3}\right) \times \frac{\sinh(\pi B^2 P_{pb}/2)}{\cosh(\pi B^2 P_{pb}/2) - \cos[2\pi(|\nu - \nu_0|/d)]}, \quad (10)$$

where $P_{pb} = (P_H + bP_m)^n$, P_H is the partial pressure of H_2-He broadening gas (roughly the total pressure), P_m is the partial pressure of the molecule producing the line spectrum, and the other parameters are constants which can be fitted to laboratory data. We replace the cosine term with zero since it varies with a frequency much higher than that of the band itself. This model assumes that the dominant mechanism determining line width is pressure-broadening, which is relevant to our study because of the high hydrogen pressure at a given temperature. Tabulations of Rosseland mean water vapor opacities in the recent literature assume thermal broadening only (Alexander, Johnson, and Rypma 1983; Alexander 1986) and are not applicable here.

The constants in equation (10) are taken from Edwards *et al.* (1967) for H_2O, CO, and CH_4, with the bandwidth parameter increased by a factor of 2 based on comparison with H_2O laboratory data of Ludwig (1971) over a range of temperatures from 600 to 2000 K. The model tends to reproduce the shape of the absorption bands of H_2O within the variation seen in laboratory studies (cf. discussion in Ludwig 1971). At hydrogen (total) pressures below 10 bars, the pressure broadening has not yet produced complete overlap of rotational lines, and the absorption coefficient due to the molecular lines goes as P. With increasing pressure, the dependence becomes progressively weaker. Because the strongest bands are formed in regions where thermal broadening may dominate (pressures below 0.1 bars), a precise treatment of the shape of these bands requires consideration of the transition between thermal and pressure broadening. This is not undertaken in the present study.

The electronic absorption bands of TiO in the visible portion of the spectrum are treated as a simple linear ramp of increasing opacity with increasing wavenumber, based on a plot in Tsuji (1971). These bands do not contribute significantly to the overall opacity except at temperatures in excess of 2000 K, for which H^- ions also provide substantial opacity; additionally, they are not important in our synthetic spectra, which are constructed for wavelengths in excess of 1 μm. A detailed band model is thus not justified for this molecule.

iii) *Condensates*

Solar-composition atmospheres with effective temperatures in the 1000–2000 K range may contain condensed phases of so-called refractory materials such as iron, sodium-aluminum silicates, and magnesium silicates. A justification of this requires construction of a temperature-pressure profile with condensation curves superposed; this exercise is illustrated in Figure 2, which shows pressure-temperature loci of condensation in a solar composition atmosphere. Superposed are temperature profiles in a 0.05 $M_\odot$, 0.1 $R_\odot$ object with $T_e = 1500$

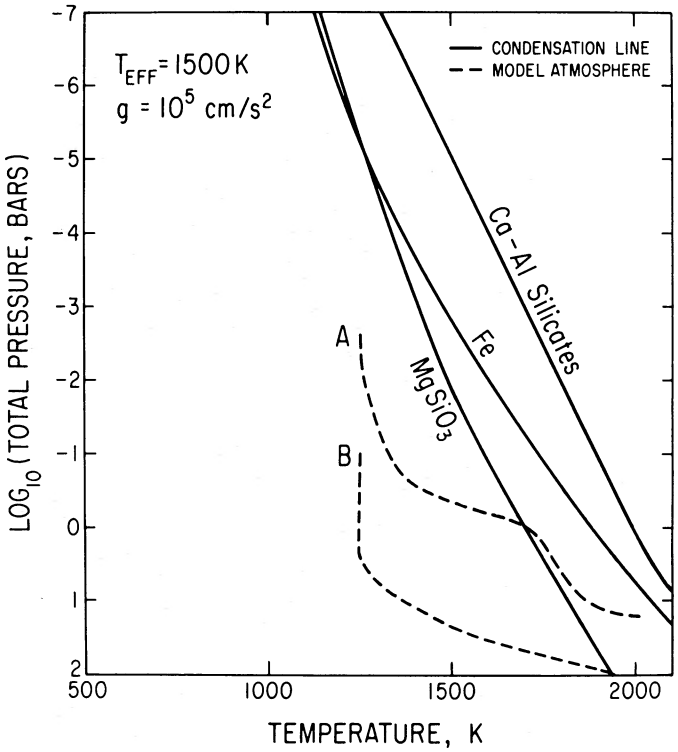

FIG. 2.—Temperature profiles computed for a hydrogen-helium atmosphere (A) with and (B) without clouds. Profile B is the Rosseland mean profile of Fig. 1; profile A assumes the dusty cloud model (Planck mean) with a single condensation level at 1 bar pressure as discussed in text. Solid lines are boundaries of condensation for the labeled constituents from Barshay and Lewis (1976), assuming no thermodynamic contact between gaseous and solid phases.

K. The condensation sequence is based on one in Barshay and Lewis (1976), which assumes that material previously condensed is not in thermodynamic contact with the remaining gas. This extreme assumption is likely to be more relevant than equilibrium condensation, since the altitude levels at which condensation of constituents occurs are spatially separated, and individual particles transported by turbulence to higher levels are likely to coagulate to micron size, inhibiting diffusion of gas into their interiors. Under these conditions the abundant high-temperature condensates are silicates of aluminum and calcium, iron/nickel, and the magnesium silicate enstatite.

Pollack, McKay, and Christofferson (1985) studied the effect of dust grains, including the constituents listed above, on opacity in the primordial solar nebula. They derived analytic expressions for absorption coefficients in the limit of small and large particles, with the size scale set by the wavelength. We show in § IV*c* that, for the situation in which the condensate vertical distribution is determined by turbulent mixing, the ratio of particle circumference to wavelength is in excess of 30. Based on the numerical results of Pollack, McKay, and Christofferson (1985), this is within the large particle, or geometric optics, limit. For the case in which the vertical cloud profile is determined by the vapor pressure, the particle size is more uncertain but plausibly is large because turbulence will be operative in the condensation zone; also, much of the material will condense out as a liquid, enhancing coalescence.

In the geometric optics limit, for any constituent which absorbs in the wavelength region of interest, the absorption cross section equals the geometric cross section, so that

$$\kappa \ (\mathrm{cm}^2 \ \mathrm{g}^{-1}) \approx (a_p \rho_p)^{-1} , \tag{11}$$

where a_p, ρ_p are particle radius and density. That this holds for the silicate and iron condensates of importance to brown dwarfs is demonstrated by the numerical calculations of Pollack, McKay, and Christofferson (1985), which show geometrical optics behavior for refractory condensates of particle size 100 μm through the temperature range of interest to us. The implication for our work is that large particles act as gray absorbers in the wavelength range 1–10 μm, with absorption coefficient ~ 50 cm^2 g^{-1}, derived from the particle sizes calculated in § IV*c*. This frequency independence is assumed in the calculations which follow. Although we feel that large particle sizes are most sensible in the brown dwarf models, we acknowledge that exploration of the effects of smaller particles may also be of interest but requires calculation of scattering processes beyond the scope of the present effort (Van de Hulst 1957).

The dependence of our spectral fits on the grayness of the cloud opacity can be gauged by anticipating somewhat our later results. We find in § VI that an atmosphere with an optically thick gray cloud can fit the two-color data on VB 8B, while an atmosphere containing only pressure-induced hydrogen absorption, which has an absorption coefficient varying by a factor of 5 from 1 to 3 μm, cannot reproduce the measured fluxes of MPL. The difference in integrated flux over each band for the two cases, at a given effective temperature, is roughly a factor of 2. Based on our experience in trying to fit the VB 8 spectra with various nongray cases, we conclude that the absorption coefficient of cloud material cannot vary by more than a factor of several over 1–3 μm in order to reproduce the data of MPL. The large-particle case satisfies this criterion; exploration of scattering cases in which the absorption coefficient varies with frequency due to either particle size or composition (Pollack, Toon, and Khare 1973) is future work.

At effective temperatures approaching those of present-day Jupiter, water and ammonia condensates occur near the unity optical depth level in a solar-composition atmosphere. They appear to play only a secondary role in determining the temperature structure but are crucial in interpreting emergent spectra of the giant planets (Bjoraker 1985).

c) Physical Model of Cloud Formation

To complete the calculation of temperature profiles in a cloudy atmosphere model, we require a model for the cloud particle size and distribution of cloud particles with height. We consider two extreme models illustrated in Figure 3: condensation clouds and dusty clouds. The condensation model assumes that the vertical profile of mass density of the condensed material is determined by the vapor pressure profile above the pressure level at which condensation begins, and is zero below that. Condensates which fall out at any given level are assumed to evaporate at lower, hotter levels and are immediately replaced by newly condensed vapor. The resulting density profile of condensate is

$$\rho_c = \begin{cases} \dfrac{P_{s,i}\,\mu_i}{RT} & (x_i P > P_{s,i}) \\ 0 & (\text{otherwise}) , \end{cases} \tag{12}$$

where x_i is the number fraction of cloud-forming constituent i taken from Anders and Ebihara (1982), μ_i is the molecular weight, and the vapor pressures based on the results of Barshay and Lewis (1976) are fitted to Clausius-Clapeyron–type relationships:

$$\begin{aligned} P_{s,\mathrm{MgSiO_3}} &= x_{\mathrm{MgSiO_3}} \exp (0.01T - 17.) , \\ P_{s,\mathrm{Fe}} &= x_{\mathrm{Fe}} \exp (0.00667T - 12.7) , \\ P_{s,\mathrm{Ca\text{-}Al}} &= x_{\mathrm{Ca\text{-}Al}} \exp (0.01T - 20.) , \end{aligned} \tag{13}$$

where $P_{s,i}$ and x_i are the saturation vapor pressure and number

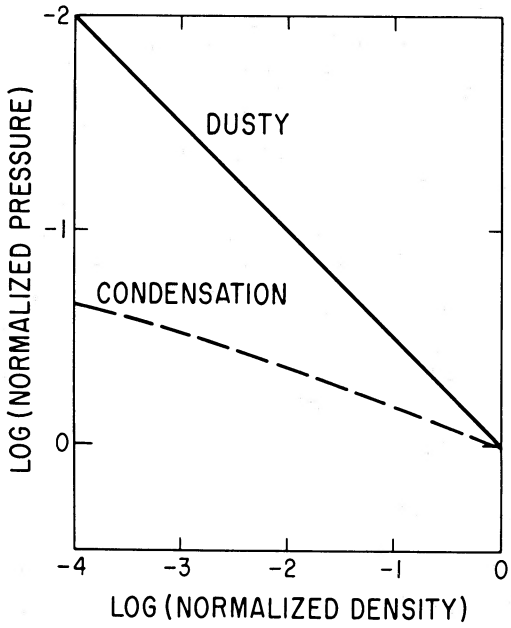

FIG. 3.—Cloud mass density profiles for the condensation (*dashed*) and dusty (*solid*) cloud models described in text, assuming a single condensate. Total pressure and cloud density are normalized to values at the deepest level at which condensation occurs, below which the cloud density is set to zero.

fraction of constituent i (Ca-Al refers to calcium and aluminum silicates).

The dusty cloud model incorporates in an approximate way transport of cloud particles by turbulence to regions well above the level at which they condensed. The cloud density is determined by an equation of the form

$$\rho_c = \rho_{c,0} \exp\left[-\left(\frac{1}{H} + \frac{w}{K}\right)(z - z_0)\right] \quad (14)$$

(Prinn and Olaguer 1981) where z and z_0 are altitude levels, w is the gravitational sedimentation velocity, H the density scale height, and K an eddy diffusion coefficient defined in the usual way (see, e.g., Hunten 1973). The above equations are strictly valid only in an isothermal atmosphere. From free convection theory (Stone 1976), the eddy diffusion coefficient can be estimated as

$$K \simeq H\left(\frac{R}{c_p \mu}\frac{\sigma T_e^4}{\rho_g}\right)^{1/3}, \quad (15)$$

where c_p is the specific heat of atmosphere. The sedimentation velocity is a function of particle size a_p and is estimated from equations for the drag force in the continuum flow regime:

$$w = \begin{cases} \left[\frac{16}{3} a_p g\left(\frac{\rho_p}{\rho_g} - 1\right)\right]^{1/2} & \left(\frac{2\rho_g w a_p}{\eta} \gg 70\right), \\ \frac{2}{9} a_p^2 g \frac{(\rho_p - \rho_g)}{\eta} & \left(\frac{2\rho_g w a_p}{\eta} \ll 70\right), \end{cases} \quad (16)$$

where the gas and particle density are ρ_g and ρ_p respectively, and η is the dynamic viscosity of the gas.

The physics of coagulation and coalescense is a complicated affair (Rossow 1978); the result is generally a power-law size spectrum of particles. Rather than compute a spectrum, we employ the above theory in an approximate way by assuming all particles coagulate or coalesce rapidly to a maximum size determined by setting the sedimentation velocity w equal to K/H, with all larger particles falling quickly to a level at which evaporation takes place. This yields a mass density of condensate which goes as the square of the gas pressure, from equation (14). The level at which condensation begins, for this model, must strictly be found by iterating an atmosphere model to find the level below which condensation does not occur, and letting the condensate density fall off as P^2 above that. To avoid multiple iterations of an atmosphere model, we set the condensation level at 1 bar pressure, which is crudely consistent with that expected for our high-luminosity brown dwarfs, i.e., T_e = 1300–1500 K (see Fig. 2).

Figure 4 plots the eddy diffusion coefficient and maximum particle radius as a function of effective temperature for two values of the gravitational acceleration. Values of K for the high-luminosity cases range from 10^9 to 10^{11} cm^2 s^{-1}, about a factor of 10–100 larger than that for the Jovian atmosphere case. The resulting maximum particle size for the higher mass brown dwarf is 50–100 μm; hence $2\pi a_p \nu \geq 30$, for wavelengths less than 10 μm, if all the particles attain this size.

d) Oxidation State of Abundant Z-Elements in Atmosphere

To complete the construction of the model atmospheres, the chemical oxidation state of the common Z-elements carbon and nitrogen must be specified. This is particularly crucial for carbon, which in a solar-composition gas is two-thirds as abundant as oxygen and therefore controls the amount of water available in the atmosphere. As shown in § VI, water has a first-order effect on the spectra of high-luminosity (candidate VB 8B) brown dwarfs.

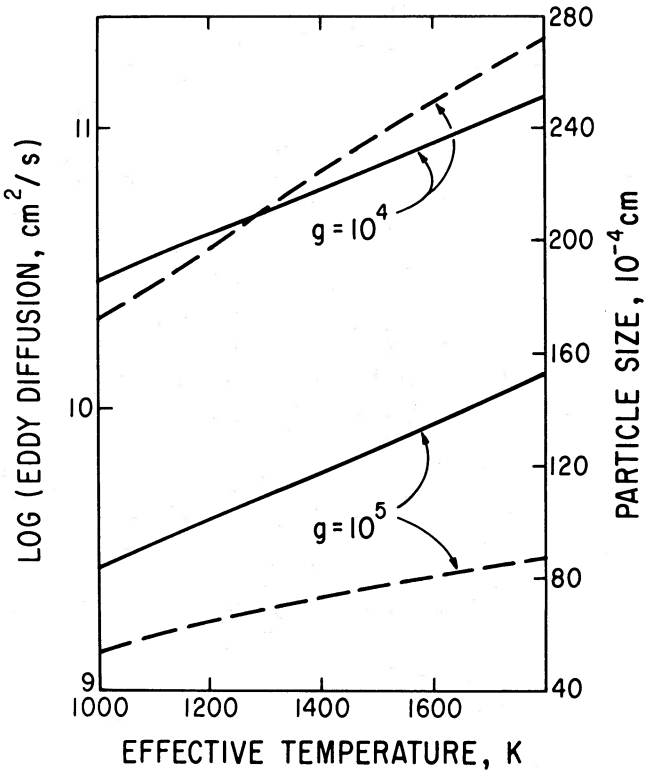

FIG. 4.—Eddy diffusion coefficient (*solid line*) and particle size (*dashed line*) as a function of effective temperature based on a model described in the text. Values of surface gravity in cgs units.

Figure 5 plots temperature versus hydrogen pressure for solar composition envelopes corresponding to Jupiter, a model gaseous nebula around the primordial Sun, a brown dwarf atmosphere of pure H_2-He, and a brown dwarf atmosphere with condensed silicates. The brown dwarf cases are calculated as described above and assume T_e = 1500 K, $g = 10^5$ cm s^{-2}; the Jupiter adiabat is tied to that body's measured luminosity, and the nebula to the composition of the present-day planets (see Barshay and Lewis 1976, from which the last two are taken for an explanation of those profiles). Also plotted from Barshay and Lewis (1976) are the temperature-pressure loci for which the abundance of CH_4 equals that of CO, and likewise for NH_3 and N_2, for solar elemental abundances (note the solar C/O ratio is not known to better than 30%). Jupiter's convective outer envelope is dominated by CH_4 and NH_3; the solar nebula model has a much higher temperature for a given hydrogen pressure and is dominated by CO and N_2. The high-luminosity brown dwarf is decidedly N_2-dominated and is marginally CO-rich at the expense of CH_4. Graphite is not stable in any of the temperature profiles shown.

Figure 6 plots the water abundance as a function of temperature at 1 bar total pressure for several different elemental ratios of O to C (all other elements being in solar abundance relative to hydrogen), using a chemical equilibrium program kindly provided by J. S. Lewis. This program and the calculations of Barshay and Lewis use equilibrium constants primarily from JANAF tables (1971) to calculate the abundance of a wide variety of gaseous molecular species for a given tem-

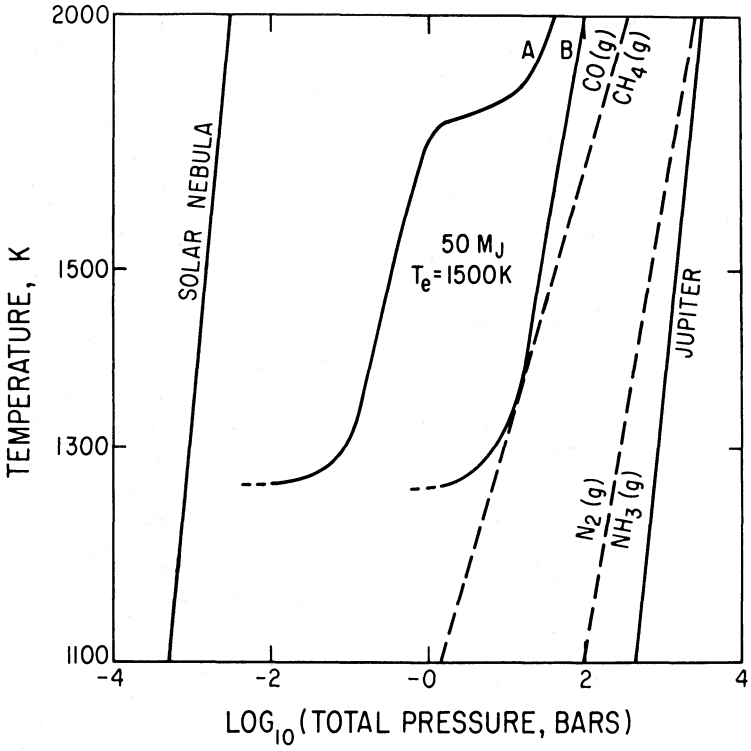

FIG. 5.—Temperature vs. pressure in the atmospheres of brown dwarf models A and B of Fig. 2, in the deep envelope of Jupiter, and in a model of the primordial gaseous nebula surrounding the Sun. Dashed lines show temperature-pressure loci at which the abundances of the indicated carbon and nitrogen species are equal. Dashed lines, Jupiter, and solar nebula profiles from Barshay and Lewis (1976).

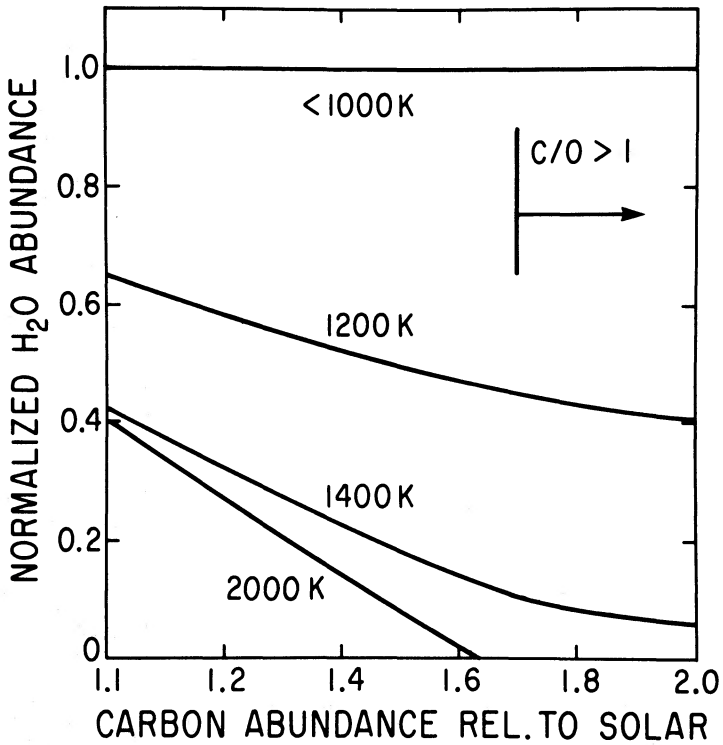

Fig. 6.—Water abundance vs. carbon abundance for several different temperatures, all at 1 bar H_2 pressure. Oxygen abundance is solar, hence abscissa is C/O ratio normalized to the solar value. Ordinate is normalized to the solar elemental oxygen abundance. C/O > 1 for abscissa values in excess of 1.7. Figure is constructed from a program provided by J. S. Lewis.

perature, total pressure, and elemental composition assuming thermodynamic equilibrium. The activity of graphite is also calculated to determine whether condensation of that material is possible. The carbon not present as CO is in all cases predominantly CH_4; thus the CO to CH_4 ratio can be derived from the figure.

Although, as shown in § IV*e*, water abundance has a secondary effect on the atmospheric temperature structure, it does dominate the appearance of the emergent spectrum; Figure 6 suggests that such spectra could be a sensitive indicator of the carbon to oxygen ratio and temperature structure in a brown dwarf atmosphere. We discuss this point more fully in § VI.

e) Model Temperature Profiles

We now present the temperature profiles based on the radiative transfer scheme and treatment of opacity sources discussed above. We focus on the effective temperature region from 1000 to 1500 K which brackets the blackbody temperature of VB 8B as derived by MPL. We will use our results later to redetermine the effective temperature and luminosity of this object. We present results for 0.05 $M_\odot$, which for an object of 0.1 $R_\odot$ yields a surface gravity of 1.3×10^5 cm s^{-2}. Models have also been run for masses down to one-tenth this value. We have already crudely justified this choice of radius from the zero-temperature equation of state discussed in § III; the interior model presented in § V provides a more detailed justification.

Figure 1 shows Planck and Rosseland mean profiles for an atmosphere with hydrogen-helium opacity only at $T_e = 1500$ K. The difference in profiles due to the different opacity averaging schemes has already been discussed in § IV*a*. Of particular interest is the effect of the shift in Plack function toward the spectral region of rapidly decreasing opacity for increasing

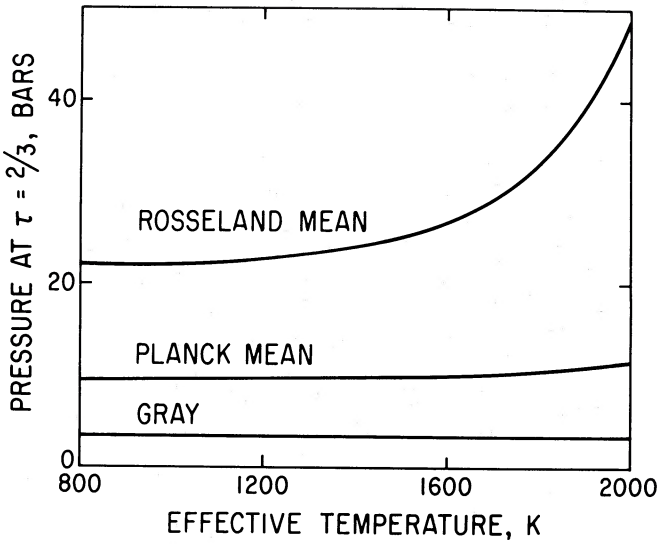

FIG. 7.—Total pressure at optical depth $\frac{2}{3}$ for an atmospheric opacity due to hydrogen and helium only (see Fig. 1). The gray atmosphere case is for a frequency-independent opacity (cm^2 g^{-1}) equal to 0.005 times pressure in bars.

effective temperature. Figure 7 plots the pressure at optical depth $\frac{2}{3}$ as a function of effective temperature in the Rosseland and Planck mean approximations.

Figure 8 compares temperature profiles for our condensation cloud and dusty cloud models, at $T_e = 1500$ K. The presence of distinct regions of high-temperature gradient is due to the sharp opacity variations between zones of condensate and those free of clouds. The boundary of the deep convection zone for high effective temperatures (above 1000 K) is deter-

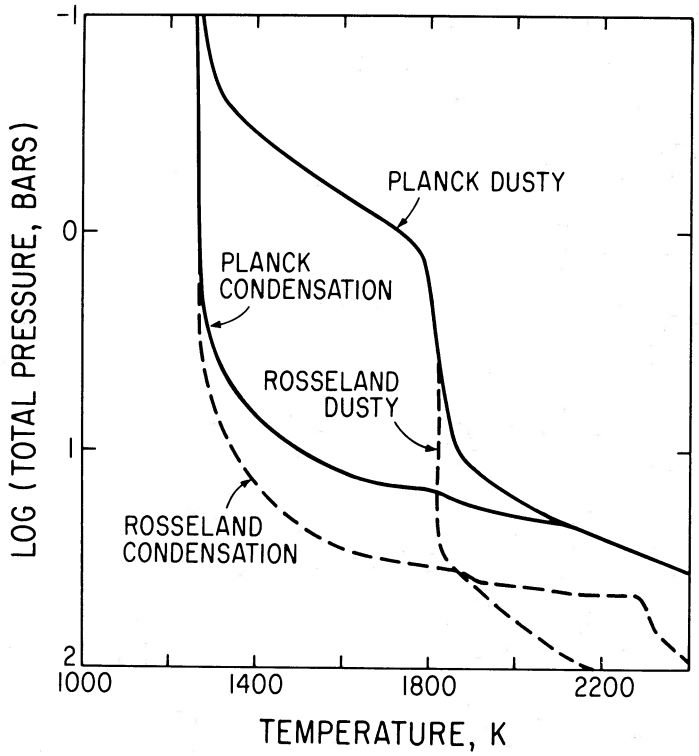

FIG. 8.—Temperature profiles in the baseline brown dwarf assuming condensation and dusty cloud opacity models, plus hydrogen-helium opacity

mined by the hydrogen-helium opacity at levels deeper than those for which condensation takes place. The effect of clouds is to raise the temperature at a given pressure level above that for the pure hydrogen-helium case, as seen by comparing Figures 1 and 8.

The effect of molecular line absorbers on the temperature profile is generally secondary to that of clouds, particularly in the Rosseland mean case, which weights the gaps between lines and bands rather than the line and band maxima themselves. Thus temperature profiles including these absorbers with no clouds fall at intermediate temperatures, for a given pressure level, between the cases shown in Figures 1 and 8.

The level at which the deep convection zone begins is of primary interest in determining the interior structure and evolution of brown dwarfs. In any case, convection dominates in regions below which hydrogen begins dissociating and pressure-ionizing, both because of increased opacity (which raises the temperature gradient) and a decrease in the adiabatic temperature gradient in the dissociating and ionizing regions (the latter effect occurring only over restricted pressure regimes). The atmospheric level at which convection begins differs somewhat in our Rosseland and Planck mean cases. In the Rosseland mean case, the convection zone begins where the abundance of H^- ions (due primarily to the presence of Z-elements in the gas) is sufficient to provide substantial opacity at wavelengths shorter than 1 μm. These effects become important above 2000 K. Since the Planck mean preferentially samples the highest opacities, the convection zone for that choice of opacity generally begins above the level at which H^- opacity becomes important.

To avoid proliferation of models, we choose three representative extreme atmospheric cases as boundary conditions for the evolution models. The coolest case is an atmosphere with only hydrogen-helium opacity, calculated in the Rosseland mean limit ("R"). As an intermediate case we calculate the same atmosphere but with opacities averaged by the Planck mean ("P"). Finally, we have the hottest case: an atmosphere with dusty cloud opacities calculated by the Planck mean ("C"). In each case, the appropriate grid of model atmospheres is represented by performing a fit of the following equation to the results of integration of the atmospheres:

$$T_{10} = AT_e^B g^C , \tag{17}$$

where T_{10} is the temperature at the 10 bar pressure level in the atmosphere, T_e is its effective temperature, g is the surface gravity, and A, B, and C are constants. The fitting point is conveniently placed at a pressure of 10 bars because at this point for the Planck mean the atmosphere is entirely within the ideal gas limit, the H_2 is still entirely undissociated for our range of effective temperatures, and the temperature gradient is closely adiabatic. This is not true for the Rosseland mean case; here T_{10} is extrapolated back along an adiabat from values at higher pressure levels.

A power-law fit for the cloudy case is not valid, since drastic changes in T_{10} must occur as the level of cloud formation passes below 10 bars with decreasing effective temperature. This effect is illustrated in Figure 9, which plots T_{10} versus T_e for the condensation cloud case. At the highest temperatures, cloud formation will not occur at all, but the effect on opacity is not evident in the figure because of the increasing importance of H^- opacity and the relatively small contribution of the condensation cloud to the total opacity. Also shown is the dusty cloud case, which only fits a power law because we have

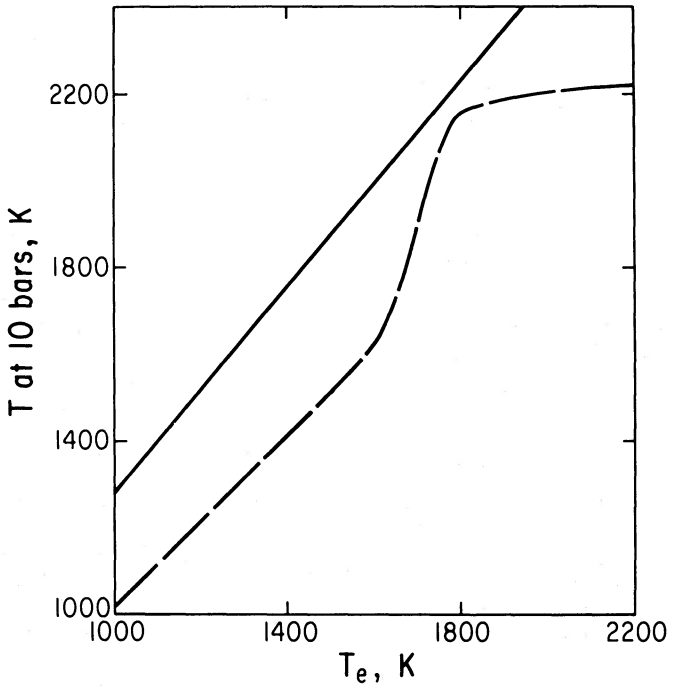

FIG. 9.—Temperature at 10 bars pressure vs. effective temperature for condensation (*dashed line*) and dusty (*solid line*) cloud models. Surface gravity is 10^5 cm s^{-2}.

fixed the cloud base to be at 1 bar pressure. This is crudely valid only in the region from 1300 to $\sim$1700 K. To calculate the actual cloud base as a function of T_e, an iterative radiative transfer scheme would have to be adopted, since the cloud material above the base is the dominant opacity source for the dusty cloud case. Such a scheme is beyond the scope of the present work. We acknowledge this limitation and regard the power-law fit labeled C as an exploration of the effect of high atmospheric opacities on the overall cooling curve calculated in § V. An accurate determination of T_{10} versus T_e for the dusty cloud case could include changes in the sign of the dependence of T_{10} on T_e, as proposed by Stevenson (1986), leading to discontinuities in the slope of the brown dwarf cooling curve. Although such effects on the cooling curve cannot be calculated in the present effort, we believe that our high-opacity case is a useful determination of the sensitivity of overall brown dwarf cooling to atmospheric opacity. Accurate characterization of cloud formation as a function of effective temperature is an important but involved issue and is planned as a future effort. To ensure that case C represents a high-opacity situation, temperatures calculated from the power law are roughly 30% higher than given by the Planck dusty cloud calculation itself. The limitation of setting the cloud-forming level at 1 bar does *not* affect our fitting of brown dwarf spectra, described in § VI, since for the best-fit effective temperatures for VB 8B, this level is roughly correct based on Figure 2.

Values for the fitting constants for the three types of atmospheric boundary conditions are given in Table 1 for T_{10} and T_e in K and g in cm s^{-2}. The power law in case C is dependent on the particular pressure level chosen for the base of the dusty cloud; a range of exponents in T_e from 0.7 to 1.0 alters the evolution curves described in § V by less than 30%.

As we see in § V, the gross properties of evolving brown dwarf models show some degree of sensitivity to the amount of

TABLE 1

MODEL ATMOSPHERE GRID PARAMETERS

	CONSTANT		
TYPE OF ATMOSPHERE	*A*	*B*	*C*
R.....	26.3	0.78	−0.17
P.....	4.4	0.98	−0.11
C.....	50.4	0.71	−0.11

atmospheric opacity; however, the order of magnitude of the calculated cooling time scales is generally insensitive to the boundary conditions.

V. INTERIOR STRUCTURE AND AGE-MASS-LUMINOSITY RELATIONS

a) *Calculation of Interior Structure*

The calculation of interior models is arranged to take advantage of the isentropic temperature profile at any instant and to provide maximum accuracy in the calculation of radius and interior density distribution. We begin by prescribing a mass and an initial value of T_e. A preliminary value of g is guessed, and then the boundary condition (17) is used to calculate T_{10}, the temperature at 10 bars pressure. The specific entropy of a solar composition gas at this fitting point is then calculated. We then calculate the relevant thermodynamic parameters (temperature T, pressure P, heat capacity per unit mass at constant volume C_V, and γ, the adiabatic variation of ln T with ln ρ) along this adiabat at a variety of densities ρ. Methods for calculating the thermodynamics are described in § V*b*. For each density point, the temperature is iterated until the specific entropy is equal, on the same zero point, to the value at the fitting point. The calculation of the adiabat is carried to progressively higher densities until we have spanned the expected range of densities in the interior model.

After the thermodynamic variables have been obtained at each specified density point, an analytic representation of each variable is generated by fitting it with a smooth polynomial to a specified accuracy of $\lesssim 1\%$. This procedure has the effect of smoothly interpolating over any phase discontinuity in the vicinity of 3 Mbar pressure. The calculation of the interior adiabat can thus be carried out without knowing the details of the transition region (Hubbard 1973; Hayashi and Nakano 1963). In our brown dwarf models, the transition region is entirely contained between the two outermost grid points and thus contributes negligibly to the bulk properties of the model.

The independent Lagrangian variable for the integration of models is taken to be the mass m enclosed within a sphere of radius r. The model is divided into 100 equally spaced mass zones. We assume an initial density profile $\rho(m)$. Then we calculate the radius of each mass zone by integrating the equation of mass conservation

$$dr^3 = 3dm/(4\pi\rho) . \quad (18)$$

The total radius of the object R is reached at the point where $m = M$, the total mass.

Next we compute the pressure at each mass zone by integrating

$$dP = -Gmdm/(4\pi r^4) , \quad (19)$$

subject to the condition that $P = 10$ bars at $m = M, r = R$. The final step in the iteration cycle is to combine the $P(m)$ profile resulting from equation (19) with the $P(\rho)$ relation for the interior adiabat to obtain a new $\rho(m)$ profile, which is then substituted into equation (18) to start a new iteration. The surface gravity g is also iterated upon for full self-consistency. The process converges rapidly, is very stable, and is inherently accurate because only integral equations rather than differential equations are solved.

After the initial model with the starting value of T_e is calculated, we decrement T_e by a specified amount (usually 5%), and a new model is calculated with this boundary condition. If the observed luminosity L is derived solely from contraction and cooling, with no contribution from nuclear reactions, we have

$$L = 4\pi R^2 \sigma T_e^4 = -\int dmC_V(dT/dt - \gamma T d(\ln \rho)/dt) , \quad (20)$$

where σ is the Stefan-Boltzmann constant and the integral is taken over all mass shells. This equation is combined with the initial model and subsequent models to determine the time interval dt between these two models. Time intervals between subsequent models are determined in the same manner.

b) *Thermodynamic Relations*

In this study we utilize a generalized thermodynamic description of electron-degenerate hydrogen-helium mixtures which was developed for use in computations of interior models of Jupiter and Saturn (MacFarlane and Hubbard 1983; MacFarlane 1984; Hubbard and MacFarlane 1985). The theory is based on extensive calculations of the energy and pressures of zero-temperature lattices of hydrogen and helium mixtures evaluated at several densities, using a three-dimensional Thomas-Fermi-Dirac theory (TFD3D). The results are then generalized to finite temperatures in two different ways: one approach uses hard-sphere perturbation theory to model the liquid-state thermodynamics of a mixture of metallic hydrogen and helium, while the other approach (Hubbard and MacFarlane 1985) models the mixture of screened nuclei in terms of a model-free energy for an unscreened two-component plasma, with density-dependent effective charges for the nuclei. The latter approach provides convenient explicit expressions for the thermodynamic variables and is used in this paper. Another alternative would be to use the formulation of Hubbard and DeWitt (1985) based on linear response theory. The differences between these various theories should be insignificant for the models discussed in this paper. They are more important for models in the Jovian planet mass range. By the same token, since our thermodynamic description is designed to be quantitatively valid for Jovian-class models, and since it is also tailored to approach ideal gas Fermi-Dirac thermodynamics in the limit of much more massive objects (white dwarfs), it should be quite accurate for the intermediate-range objects considered here.

As described above, the liquid-state TFD3D results are used to provide values of thermodynamic parameters along a specified isentrope, for a fixed helium abundance (we use a helium mass fraction $Y = 0.2$), over the entire density range covered by a given interior model. We find that, for the temperatures of interest in this study, it is not necessary to include corrections for quantization of the degrees of freedom of the protons and helium nuclei. That is, the system can to good approximation be treated as a classical liquid. It follows that there is no significant reduction in the liquid-state heat capacity due to quantum freeze-out of degrees of freedom. Phrased differently, temperatures are always well above the effective Debye temperature.

TABLE 2

EVOLUTIONARY SEQUENCES

T_e (K)	P BOUNDARY CONDITION				R BOUNDARY CONDITION				C BOUNDARY CONDITION			
	R[a] (10^4 km)	T_c[b] (10^6 K)	ρ_c[c] (g cm^{-3})	t (10^9 yr)	R[a] (10^4 km)	T_c[b] (10^6 K)	ρ_c[c] (g cm^{-3})	t (10^9 yr)	R[a] (10^4 km)	T_c[b] (10^6 K)	ρ_c[c] (g cm^{-3})	t (10^9 yr)
					$\dot{M} = 1000 \times 10^{30}$ g							
2200....	7.08	1.580	340	0.00	6.36	1.223	463	0.00	9.35	1.894	151	0.00
2090....	6.98	1.542	354	0.03	6.31	1.192	474	0.02	8.79	1.865	181	0.05
1985....	6.88	1.504	368	0.06	6.27	1.161	485	0.04	8.35	1.819	211	0.12
1886....	6.79	1.465	382	0.10	6.22	1.131	496	0.07	8.05	1.781	234	0.17
1791....	6.71	1.426	395	0.15	6.18	1.101	506	0.10	7.83	1.748	254	0.24
1702....	6.64	1.386	408	0.21	6.14	1.071	517	0.14	7.66	1.722	271	0.31
1617....	6.57	1.347	422	0.28	6.10	1.041	528	0.19	7.51	1.699	287	0.38
1536....	6.50	1.307	435	0.37	6.06	1.012	538	0.25	7.39	1.672	300	0.47
1459....	6.43	1.268	448	0.48	6.03	0.983	548	0.32	7.29	1.645	313	0.57
1386....	6.37	1.229	461	0.60	5.99	0.954	558	0.41	7.19	1.618	325	0.69
1317....	6.31	1.190	474	0.76	5.96	0.925	568	0.52	7.11	1.590	336	0.83
1251....	6.26	1.151	488	0.94	5.92	0.896	577	0.64	7.03	1.563	347	1.00
1188....	6.20	1.114	501	1.17	5.89	0.866	587	0.79	6.96	1.535	357	1.20
1129....	6.15	1.077	515	1.44	5.86	0.836	596	0.97	6.89	1.507	367	1.44
1072....	6.10	1.041	528	1.75	5.83	0.804	605	1.19	6.82	1.479	377	1.72
1019....	6.05	1.005	540	2.14	5.81	0.772	614	1.45	6.76	1.450	387	2.07
968....	6.01	0.970	553	2.59	5.78	0.737	622	1.76	6.71	1.421	397	2.50
919....	5.97	0.935	564	3.12	5.75	0.696	630	2.14	6.65	1.393	406	3.01
873....	5.93	0.899	576	3.77	5.73	0.663	638	2.59	...	...	...	...
830....	5.89	0.862	588	4.55	5.71	0.636	645	3.11	...	...	...	...
788....	5.85	0.822	600	5.51	...	...	...	...	...	...	...	...
					$M = 50 \times 10^{30}$ g							
2200....	8.70	0.724	85	0.000	7.69	0.610	120	0.000	...	...	...	...
2090....	8.52	0.710	90	0.005	7.62	0.598	123	0.003	...	...	...	...
1985....	8.37	0.696	95	0.011	7.55	0.586	127	0.007	13.58	0.764	22	0.000
1886....	8.23	0.682	100	0.017	7.49	0.574	130	0.012	11.82	0.806	34	0.015
1791....	8.10	0.668	104	0.025	7.43	0.562	133	0.018	10.64	0.814	47	0.036
1702....	7.99	0.654	108	0.035	7.38	0.550	136	0.025	10.04	0.798	56	0.055
1617....	7.88	0.640	112	0.047	7.32	0.537	139	0.034	9.62	0.778	63	0.074
1536....	7.78	0.625	116	0.061	7.27	0.525	141	0.045	9.33	0.762	69	0.095
1459....	7.69	0.611	120	0.079	7.22	0.513	144	0.057	9.10	0.749	75	0.114
1386....	7.61	0.596	124	0.100	7.18	0.500	147	0.073	8.91	0.738	79	0.137
1317....	7.53	0.581	128	0.125	7.13	0.488	150	0.091	8.75	0.728	84	0.162
1251....	7.45	0.566	132	0.156	7.09	0.476	153	0.113	8.61	0.717	87	0.191
1188....	7.38	0.551	135	0.193	7.05	0.464	155	0.140	8.49	0.707	91	0.224
1129....	7.31	0.535	139	0.239	7.01	0.453	158	0.173	8.38	0.697	95	0.264
1072....	7.25	0.520	143	0.294	6.98	0.441	161	0.212	8.28	0.687	98	0.311
1019....	7.19	0.505	146	0.360	6.94	0.429	163	0.259	8.18	0.677	101	0.368
968....	7.14	0.490	150	0.440	6.91	0.417	166	0.315	8.09	0.667	104	0.437
919....	7.08	0.475	153	0.534	6.87	0.404	168	0.384	8.01	0.657	107	0.520
873....	7.03	0.460	156	0.649	6.84	0.392	171	0.466	7.93	0.646	110	0.621
830....	6.99	0.445	160	0.785	6.81	0.379	173	0.565	7.86	0.636	113	0.745
788....	6.94	0.431	163	0.944	6.78	0.366	176	0.685	7.78	0.625	116	0.895
					$M = 30 \times 10^{30}$ g							
2200....	10.00	0.421	32	0.000	8.70	0.360	48	0.000	...	...	...	...
2090....	9.75	0.411	34	0.002	8.61	0.354	49	0.001	...	...	...	...
1985....	9.52	0.401	37	0.003	8.51	0.348	51	0.002	...	...	...	...
1886....	9.33	0.393	39	0.005	8.43	0.342	52	0.004	...	...	...	...
1791....	9.16	0.385	41	0.008	8.34	0.335	54	0.005	...	...	...	...
1702....	9.00	0.377	43	0.010	8.27	0.329	55	0.007	13.22	0.455	14	0.000
1617....	8.86	0.369	45	0.013	8.19	0.322	56	0.010	12.09	0.462	18	0.007
1536....	8.73	0.362	47	0.018	8.12	0.316	58	0.013	11.31	0.456	22	0.015
1459....	8.61	0.354	49	0.023	8.06	0.310	59	0.017	10.77	0.445	26	0.024
1386....	8.49	0.346	51	0.029	8.00	0.303	60	0.021	10.40	0.434	28	0.034
1317....	8.39	0.339	53	0.036	7.94	0.297	62	0.026	10.12	0.424	31	0.043
1251....	8.29	0.331	55	0.045	7.89	0.290	63	0.033	9.90	0.416	33	0.053
1188....	8.20	0.323	56	0.056	7.83	0.284	64	0.041	9.71	0.409	35	0.064
1129....	8.11	0.315	58	0.069	7.78	0.277	65	0.051	9.54	0.402	37	0.076
1072....	8.03	0.307	60	0.085	7.74	0.271	66	0.063	9.40	0.396	38	0.090
1019....	7.96	0.299	61	0.104	7.69	0.264	67	0.077	9.26	0.390	40	0.106
968....	7.89	0.291	63	0.127	7.65	0.258	68	0.095	9.14	0.384	41	0.126
919....	7.83	0.283	64	0.155	7.61	0.252	69	0.115	9.03	0.379	43	0.150
873....	7.77	0.275	66	0.189	7.57	0.245	70	0.140	8.92	0.373	44	0.178
830....	7.71	0.267	67	0.230	7.54	0.239	71	0.170	8.82	0.367	46	0.213
788....	7.66	0.259	68	0.278	7.50	0.233	72	0.206	8.73	0.362	47	0.256

[a] At 10 bar pressure level.
[b] Central temperature.
[c] Central density.

c) Results of Calculations

We have calculated evolutionary tracks for three representative brown dwarf masses, starting with effective temperatures corresponding to the upper limit of validity of our model atmosphere grids. In general this corresponds to $T_e = 2200$ K, except for the C models, for which grain formation does not occur much above $T_e \approx 2000$ K. For these models we chose slightly lower starting temperatures. These upper limits on the effective temperature are an important restriction to the applicability of the present series of models, which will be removed in future work when the effects of molecular dissociation in the atmospheric boundary condition are quantitatively accounted for and more detailed cloud formation models are constructed. However, we argue that the evolutionary phases when such effects must be taken into account are in general of relatively brief duration ($\lesssim 10^9$ yr for the most massive models considered here) compared with the cooling times of the most evolved models. Note, though, that the evolutionary time t for all the models is the time elapsed after the starting model of the sequence. Only near the end of the sequence, when the evolution has markedly decelerated, should t be identified with the object's total age since formation. Some important parameters of the evolutionary sequences are presented in Table 2.

Figures 10–14 plot a number of properties of the brown-dwarf models. Figure 10 shows the evolutionary tracks on a theoretical Hertzsprung-Russell diagram, together with the location of V8 8B as determined by MPL and a probable error box for its location based on our model atmospheres. The trajectories correspond to cooling at nearly constant radius. Figure 11 shows the behavior of the luminosity as a function of time, together with the MPL estimate of the luminosity of V8 8B. The initial curvature in the cooling curves is an artifact of the arbitrary choice of the time zero point. Figure 12 shows the effective temperature as a function of time, again with the VB 8B value shown for comparison. Figure 13 shows the time variation of the radius. This figure displays the substantial temperature dependence of the radius. The C models, which have the hottest interior for a given mass and T_e, are substantially thermally expanded compared with the other models. Finally, Figure 14 shows the variation of the central temperature with time. This parameter is the most significant for determining the rate of hydrogen fusion at the center. Note that all our models have declining central temperatures. For comparison, we show calculations of the central temperature as a function of time for a minimum-mass (0.085 $M_\odot$) hydrogen-burning model (Graboske and Grossman 1971). Consistent with these results, our most massive model ($M = 0.050\ M_\odot$) has central temperatures which are well below the values required for hydrogen fusion.

d) Deuterium Burning

Deuterium burning is a transient phase which occurs when interior temperatures and densities are sufficiently high to cause the nuclear reaction

$$^2\mathrm{D}(p, \gamma)^3\mathrm{He}$$

to progress at a rapid rate. With the possible exception of the very lowest mass models, this reaction takes place late in the collapse phase of the brown dwarf at $T_e > 2200$ K. Hence, for most evolutionary models starting at $T_e = 2200$ K the deuterium burning phase has passed, the deuterium supply is exhausted, and the reaction does not supply energy into the

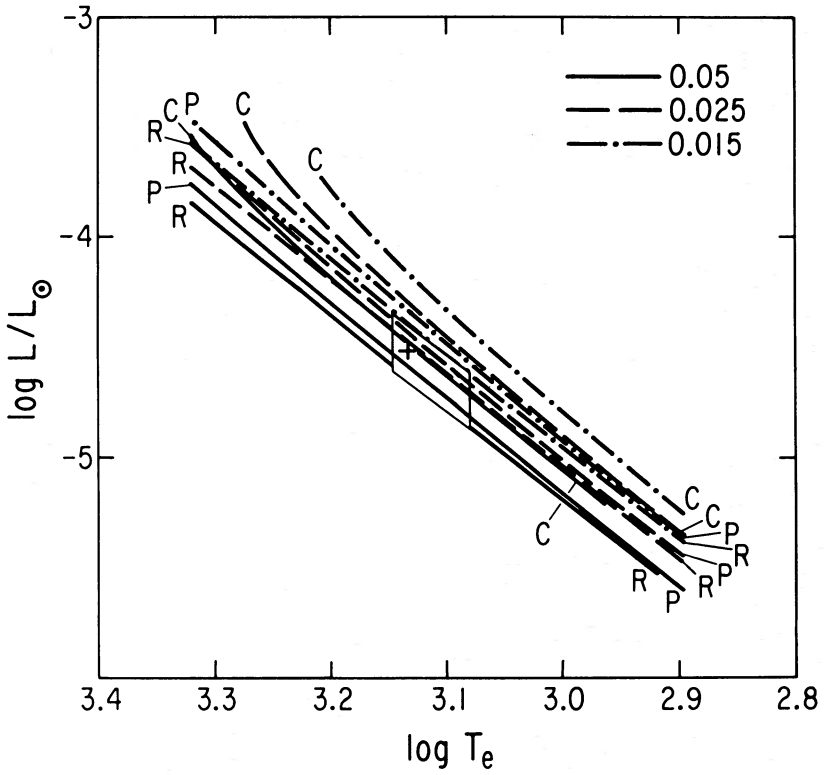

FIG. 10.—Luminosity (in $L_\odot$) vs. effective temperature for brown dwarfs with masses (in $M_\odot$) indicated. Letters label different opacity choices as described in text. Box encloses objects 10^9 yr old with effective temperatures in the range 1200–1400 K; plus indicates VB 8B values, assuming a blackbody, as reported by MPL.

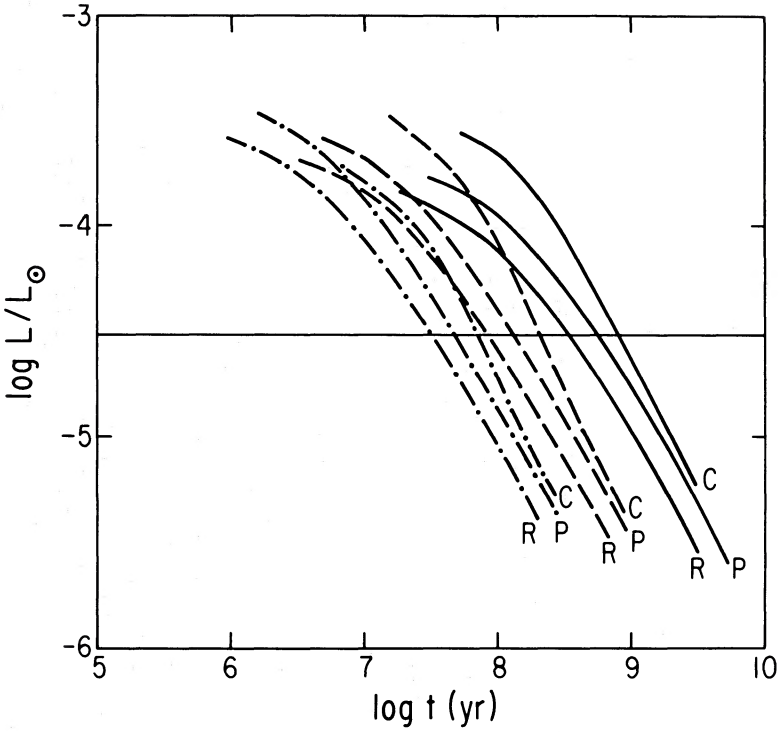

FIG. 11.—Luminosity vs. age of brown dwarfs, with symbols as in Fig. 10. Horizontal line indicates VB 8B luminosity reported by MPL, assuming a blackbody.

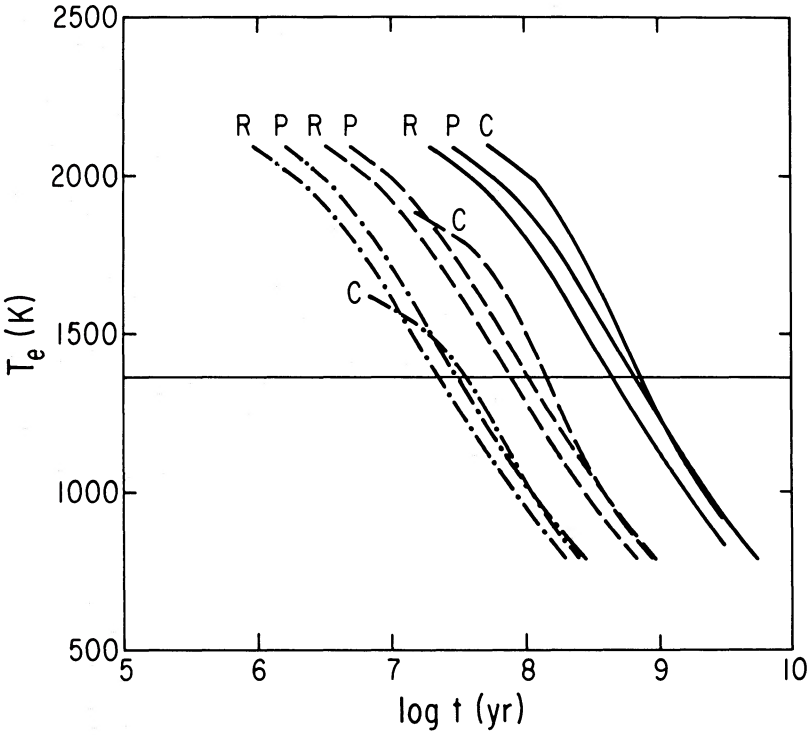

FIG. 12.—Effective temperature vs. age; symbols as in Figs. 10 and 11

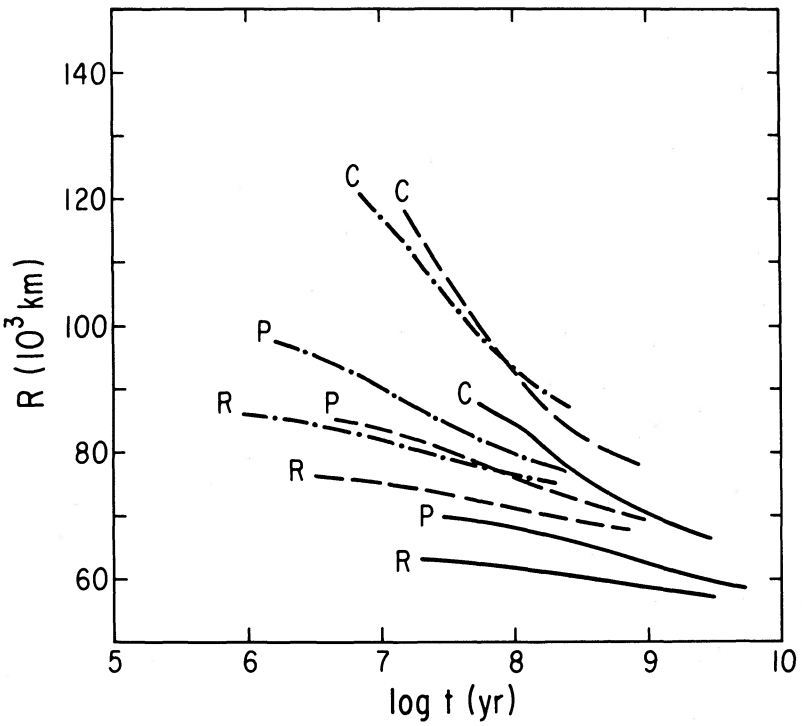

Fig. 13.—Radius vs. age; symbols as in Fig. 10

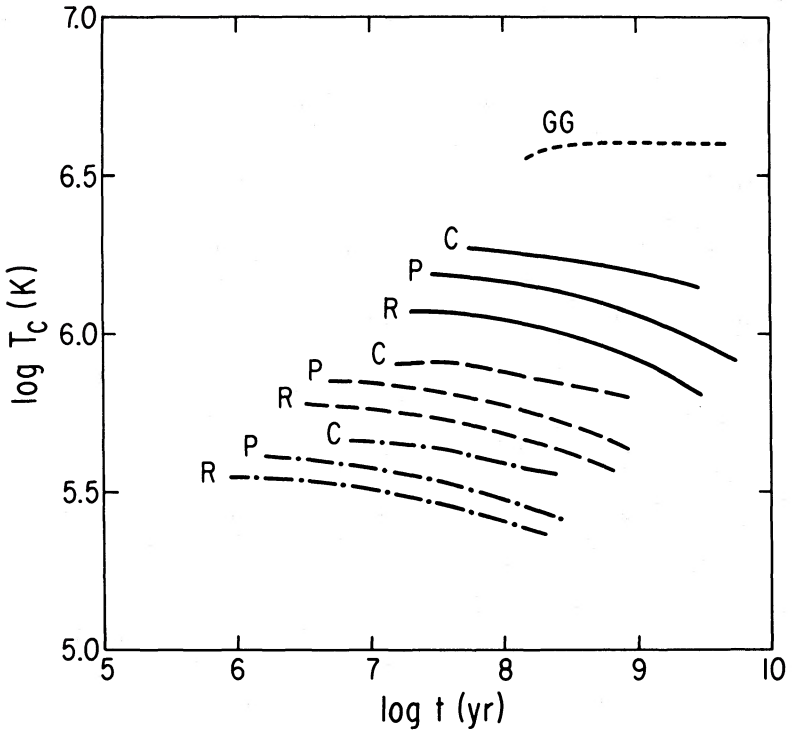

FIG. 14.—Central temperature vs. age; symbols as in Fig. 10. Line labeled GG indicates temporal behavior of an object with the minimum mass (0.085 $M_\odot$) necessary to sustain hydrogen fusion, based on Graboske and Grossman (1971).

interior of the object. The deuterium reaction may, however, be important to the smaller masses in our temperature range, since they may reach a peak central temperature at an effective temperature close to 2200 K. For this reason, and to better constrain the minimum mass for deuterium burning, particular attention was paid to the reaction in the mass range of 0.015–0.020 $M_\odot$.

The minimum mass for deuterium burning was investigated by Grossman and Graboske (1973) based on the composition $X = 0.68$, $Y = 0.29$, and $X_D = 1.9 \times 10^{-4}$, where X_D is the deuterium mass fraction. The reported minimum mass of an object for which the deuterium fusion reaction provided the predominant luminosity source at some point was 0.012 $M_\odot$. The duration of this phase was 7.5×10^7 yr for the minimum-mass object. The cosmic abundance of deuterium is now believed to be about a factor of 5 lower than assumed by Grossman and Graboske, which suggests a larger minimum mass for deuterium burning.

In our analysis of the deuterium reaction, we used the rate expression from Clayton (1968) and $X_D = 3.6 \times 10^{-5}$. In the temperature and density range of interest, the Coulomb energy of neighboring ions is of the order kT, where k is Boltzmann's constant. Hence, neither the weak nor the strong electron screening formula applies for the evaluation of the screening factor f in the thermonuclear reaction rate expression. Since f is of order unity and we are most interested in the magnitude of the reaction rate, we approximate $f = 1$. To find the minimum mass for deuterium burning, the magnitude of the nuclear energy production was evaluated at $T_e = 2200$ K. The deuterium-burning potential of objects at higher effective temperatures was approximated without the benefit of accurate atmospheric boundary conditions.

The minimum-mass deuterium-burning model evaluated at 2200 K with the Planck mean boundary condition is 0.016 $M_\odot$. Allowing for higher effective temperatures (below $T_e \approx$ 3000 K) brings the limit down to 0.015 $M_\odot$. The corresponding mass range in the Rosseland mean case is 0.017–0.018 $M_\odot$. Deuterium burning never provides more than 1% of the luminosity of smaller objects on a time scale of 10^5–10^6 yr. Larger objects will derive a significant portion of their luminosity from the nuclear reaction until the deuterium is exhausted. Taking the Planck mean result, our best estimate of the minimum mass for deuterium burning is 0.015 $M_\odot$, a value ~25% greater than the result of Grossman and Graboske (1973).

At these masses the objects quickly exhaust their deuterium supply in several times 10^6 yr. Larger objects have completed the phase when they reach $T_e = 2200$ K. Hence, deuterium burning does not significantly delay the onset of degenerate cooling and is not further considered in the evolutionary calculations.

VI. BROWN DWARF SPECTRA

Although the choice of atmospheric opacity sources does not greatly change the evolution times for degenerately cooling brown dwarfs, it does have a dominant effect on the spectral distribution of flux coming from such objects. The data of MPL, consisting of flux in two wavelength bands, contain enough information to make a crude assessment of the atmospheric composition of VB 8B. It is likely that broad-band spectra spanning the infrared could be collected in the next decade, making possible a more definitive determination of composition from the models we present in this section.

The spectra are constructed from the temperature profiles and opacity models of § IV, using equation (2). Because only crude band models are used to describe the gaseous opacity sources, we restrict ourselves to low-resolution spectra, i.e., $\Delta\nu = 300$ cm^{-1}. This is adequate both for analysis of the MPL data, for which $\Delta\nu = 600$ cm^{-1}, and for observations anticipated in the near future, which are likely to be of low to moderate resolution.

a) Effect of Temperature Profile on Spectra

Figure 15 plots flux versus wavenumber for a hydrogen-helium atmosphere at an effective temperature of 1500 K, for a 0.05 $M_\odot$, 0.1 $R_\odot$ brown dwarf. The two spectra correspond to temperature profiles computed from Planck and Rosseland mean opacities. Also shown for reference is a 1500 K blackbody curve. The dominant features in both spectra are the so-called 5 μm window of low hydrogen absorption, and the absorption falloff toward 1 μm. The Planck mean curve shows higher flux at high wavenumbers because the temperature profile is steeper than in the Rosseland mean case; hence the low-opacity windows sample higher temperatures at a given

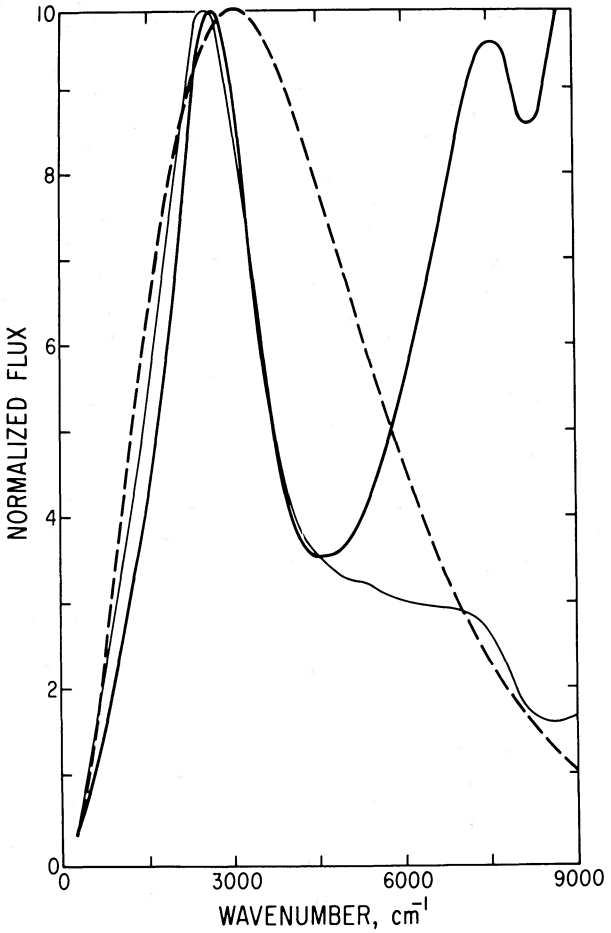

FIG. 15.—Spectral distribution of emergent flux from the atmosphere of the baseline model brown dwarf, $T_e = 1500$ K, with hydrogen-helium opacity only, plotted as normalized flux vs. wavenumber. To facilitate comparison of flux distribution, each curve is separately normalized, with maximum flux assigned a value of 10. Heavy solid line indicates temperature structure computed using Planck mean opacity; light solid line, Rosseland mean. Dashed spectrum is a gray atmosphere model.

pressure in the Planck mean case. We have not incorporated the adiabatic temperature gradient in either profile; in fact, the Planck mean case becomes convective at pressure levels for which the window regions have not yet become optically thick. The Planck mean case therefore overestimates the flux coming from the low-opacity spectral regions. The Rosseland mean underestimates the flux somewhat because it exhibits a temperature profile somewhat shallower than the adiabat, which would be obtained at lower pressure levels than the Rosseland mean case predicts. For analysis of the MPL data on VB 8B, we use spectra for both Rosseland and Planck mean profiles; the derived parameters for VB 8B do not vary much for the two extreme cases.

It should also be noted that the temperature profile at very low pressures in our model atmospheres used to calculate the emergent spectra asymptotically approaches the gray atmosphere skin temperature, rather than the lower value computed using equation (7). This overestimates the flux in spectral regions with very large opacities. The flux in these regions must in any case be small compared to that at other wavelengths; hence the appearance of the spectra presented in the figures to follow should not be affected by use of the gray skin temperature. Likewise, the analysis of the MPL data, which were taken in regions of the spectrum of relatively low opacity, is not affected.

b) *Effect of Cloud Condensates*

Figure 16 plots the spectrum of our baseline brown dwarf for the condensation cloud and dusty cloud models, at $T_e = 1500$ K; this can be compared directly with the pure hydrogen-helium Rosseland mean case of Figure 15. The presence of a broad layer of cloud in the dusty case produces a spectrum which is more nearly gray than the condensation cloud case, due to the much more extensive region of particulates at pressures too low for the gas opacity to be important. Of particular interest is the slope of the spectrum in the region from 3000 to 7000 cm^{-1}, which covers the data of MPL. The flux ratio in two broad bands measured in this region would produce rather different answers for the effective temperature, depending on the model adopted. In the absence of information on the radius of the observed object, it would not be possible to choose between the two effective temperatures. The modeling of § V provides a well-constrained radius which, along with the distance to VB 8B, provides absolute fluxes in the bands observed by MPL. We can therefore distinguish between models by fitting absolute fluxes rather than flux ratios and derive useful compositional information on VB 8B. Before doing so, it is of interest to consider the effect of molecular line absorptions on the spectrum.

c) *Effect of Atmospheric Oxidation State*

Figure 17 plots flux versus wavelength for the dusty cloud atmosphere, now also containing a solar abundance of oxygen and carbon. Also plotted is the spectrum obtained for C/O > 1, for which essentially no H_2O is present in the atmosphere. Because of the great variation in absorption strength between different H_2O and CO bands and of lines within each band, some portions of the bands are formed at pressure levels dominated by thermal broadening, and others at levels dominated by pressure broadening. The shape and precise depth of bands in Figure 17 should therefore be regarded as approximate. However, the difference in the two spectra, even in the presence of clouds, is clear. It is also apparent that intermediate

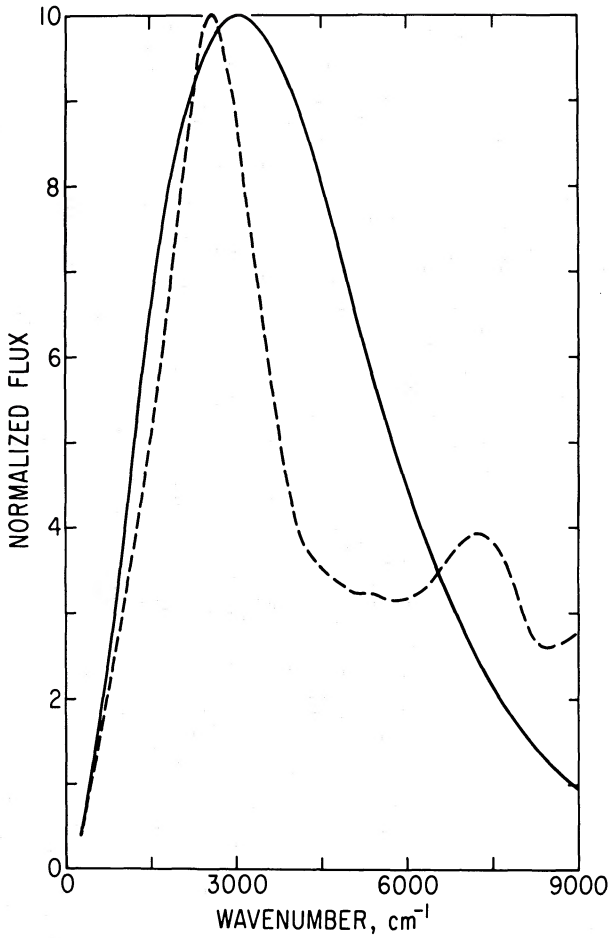

FIG. 16.—Same as Fig. 15, for condensation (*dashed line*) and dusty (*solid line*) cloud models. Temperature structure is computed using Rosseland mean.

cases, in which C/O ≈ 1, could be distinguished in a broad-band spectrum. The sensitivity of atmosphere models to the C to O ratio has been explored in red giant stars (Johnson 1982), where the molecular line opacities are important in determining the temperature structure in the absence of H_2 pressure-induced opacity. The sensitivity of the spectrum to C/O is absent in Jovian planets, since carbon is almost fully reduced in these much cooler objects.

The atmospheric oxidation state will affect the abundance and composition of silicate clouds in a brown dwarf atmosphere; also, graphite formation is thermodynamically favored for carbon abundances somewhat higher than those considered here (Lewis and Nye 1979). Graphite could be an important source of gray opacity in carbon-rich brown dwarfs. These effects, which may yield additional diagnostics in the mid-infrared for the C to O ratio, will be explored in later work.

d) *Effective Temperature and Luminosity of VB 8B*

Table 3 gives the emergent fluxes in the *H* and *K* bands derived from the dusty cloud models, using Rosseland mean opacities for $T_e = 1200$ and 1400 K. The radii requird to fit the VB 8B data of MPL are then listed for each band, the range due to the quoted uncertainty of MPL. The overlap in radii for the two bands indicates acceptable solutions. From running a range of models, at varying effective temperatures, presence of

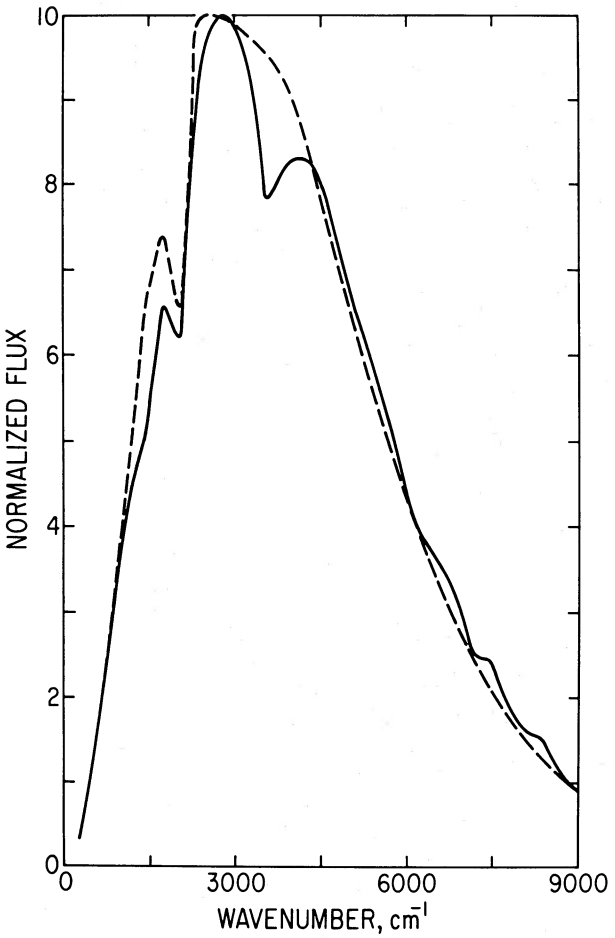

FIG. 17.—Same as Fig. 16 dusty cloud model, with gaseous water and carbon monoxide added. Dashed line indicates spectrum for which C to O ratio is in excess of unity (no water); solid line is spectrum for a solar C to O abundance.

clouds, and Rosseland versus Planck mean opacities, we conclude the following: (1) The effective temperature of VB 8B is close to that derived by MPL; acceptable fits in both Planck and Rosseland mean runs are $T_e = 1200$–1500 K. (These effective temperatures are the input values, defined in eqn. [1]. The output effective temperatures from eq. [4] are then $\lesssim 10\%$ lower and higher in the Rosseland and Planck mean cases respectively.) Outside this range, no overlap occurs in the radii determined separately from the H- and K-band fluxes. The derived radii range from 0.10 to 0.15 $R_\odot$ in the Rosseland mean case, consistent with the results of our interior models. (2) The H- and K-band data can be fitted with either a blackbody (MPL) or the *dusty* cloud model. An atmosphere with molecular absorbers only cannot fit both the ratio and magnitudes of the H- and K-band fluxes because of the sharp falloff in opacity from 4000 to 7000 cm^{-1}. For the same reason, a condensation cloud model does not fit because it provides insufficient gray absorber above the level at which the nongray pressure-induced hydrogen absorption is significant. (A small particle size for the condensation cloud case would permit higher opacities through multiple scattering but would also introduce some frequency variation in the absorption coefficient). In either the cloud-free or the condensation cloud case, no overlap in H and K radii occurs, or the overlap is at radii which are unreasonable from the point of view of the interior models (<0.09 $R_\odot$ or >0.15 $R_\odot$). Only an atmosphere with substantial cloud opacity can provide the correct slope in the observed frequency region *and* reproduce the magnitude of the fluxes. (3) A much hotter ($T > 2000$ K), late main sequence object with a large radius cannot fit the H to K ratio; a very cool ($T \lesssim 1000$ K) degenerate object could reproduce the H to

TABLE 3

DERIVED LUMINOSITY OF VB 8B

PARAMETER	T_e (K) 1200	1400
K-band emergent flux (10^6 ergs cm^{-2} s^{-1})	5.2	10.
Corresponding radius using MPL data ($R_\odot$) ..	0.14–0.16	0.10–0.11
H-band emergent flux (10^6 ergs cm^{-2} s^{-1})	2.5	6.0
Corresponding radius ($R_\odot$)	0.14–0.17	0.095–0.10
Radius overlap	0.14–0.16	0.10
Predicted luminosity (10^{-5} $L_\odot$)	3.4–4.2	3.4

NOTE.—Model runs reported are for a surface gravity of 9.3×10^4 cm s^{-2}.

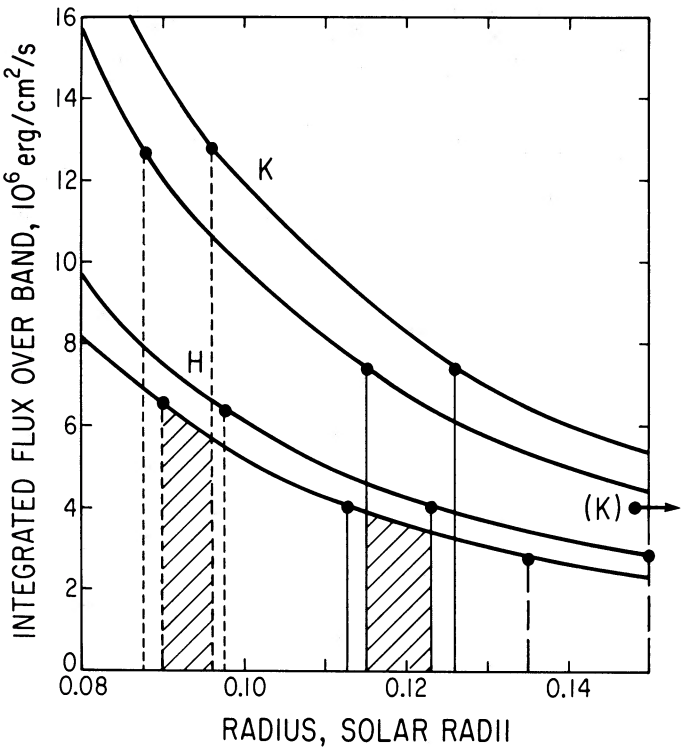

FIG. 18.—Constraints on fitting model atmospheres to VB 8B, plotted as emergent flux integrated over band vs. radius of object. Curved regions show allowed H and K flux values as a function of object radius, based on the MPL data and calibration provided by D. W. McCarthy, Jr. (1985, personal communication). Vertical lines are fluxes computed from model atmospheres, positioned within the regions allowed by the data. Overlap of resulting radii for H and K bands indicates acceptable solution. For a 1370 K blackbody (*shading bounded by short-dashed lines*), this yields a radius of 0.09 to 0.095 $R_\odot$, as noted by MPL. For a 1300 K model with hydrogen-helium and dusty cloud opacity (Rosseland mean; *shading bounded by solid lines*), the radius is roughly 0.12 solar radii. With no cloud present (*long-dashed lines*), the radii determined from the H and K bands do not overlap. See text for range of fitting exercise and conclusions drawn.

K ratio with molecular opacity sources which fall off with increasing wavenumber but requires unreasonably large radii based on the results of the interior models. The dusty cloud models can be fitted to the VB 8B data either with or without H_2O and CO present, although the acceptable range of effective temperature is narrowed somewhat by the presence of these absorbers which contribute some opacity above the clouds. To precisely assess the effect of these species on the spectrum, a band model is needed which accurately reproduces the slope of the molecular bands. The present model is felt to be too crude to satisfy this need; a more accurate model is work in progress.

Figure 18 illustrates schematically the above constraints. The narrow range within which the radius can lie provides the tightest constraint on the effective temperature of VB 8B. Note that the radius derived by MPL from their data *assuming* a blackbody is close to the value we calculate from the interior models; hence we must fit VB 8B with a spectrum which either (*a*) is close to a blackbody at 1360 K, or (*b*) mimics the H and K fluxes while being very nongray in other bands. The absorbers studied here either are gray in the region from 4000 to 7000 cm^{-1} or fall off in opacity toward higher wavenumbers. Choice (*a*) is therefore more likely to be the case than (*b*). This analysis depends on the argument that the clouds absorb as gray bodies, as discussed in § IV. Also, we have not considered minor molecular species which could affect the opacity within the H- and K-band regions.

Based on Figure 11, the derived luminosity for VB 8B corresponds to an age of order 10^9 yr for a 0.05 $M_\odot$ object, decreasing rapidly with decreasing mass. Just the luminosity measured in the H and K bands (assuming the radius derived from interior models) constrains the mass to be greater than 0.03 $M_\odot$ if the object is to be more than 10^9 yr old.

VII. EVOLUTION OF BROWN DWARFS

Figure 19 plots effective temperature versus mass for degenerately cooling objects at an age of 10^9 yr. Indicated are the major compositional and structural changes encountered during the evolution, chosen because they affect the evolution timescale or have a major effect on the emergent spectra of these objects or both. These "chemical signposts" are potentially key indicators of a particular object's age and composition and point to the desirability of obtaining broad-band infrared spectra of newly discovered degenerate objects such as VB 8B. Stevenson (1986) has raised the possibility that changes in slope of the cooling curves could occur at these signposts due to the accompanying drastic opacity changes. The overall shape of the curve is not, however, altered. In our own solar system, differentiation of helium in Saturn and possibly Jupiter is one such signpost which can be studied by remote sensing (see Conrath *et al.* 1984).

With regard to VB 8B, our modeling confirms the assessment of MPL that they observed an object near the high-mass end of the degenerate object mass spectrum. The H- and K-band data hint at the presence of refractory condensates in the visible envelope of this object. D'Antona and Mazzitelli (1985) argue that VB 8B is much older than a few times 10^9 yr and must therefore undergo hydrogen fusion in its core over limited intervals of time. Leaving aside the question of age, detailed modeling of the evolution of such a "marginal" main-sequence object requires very careful treatment of atmospheric opacity and interior physics. This is the subject of future work.

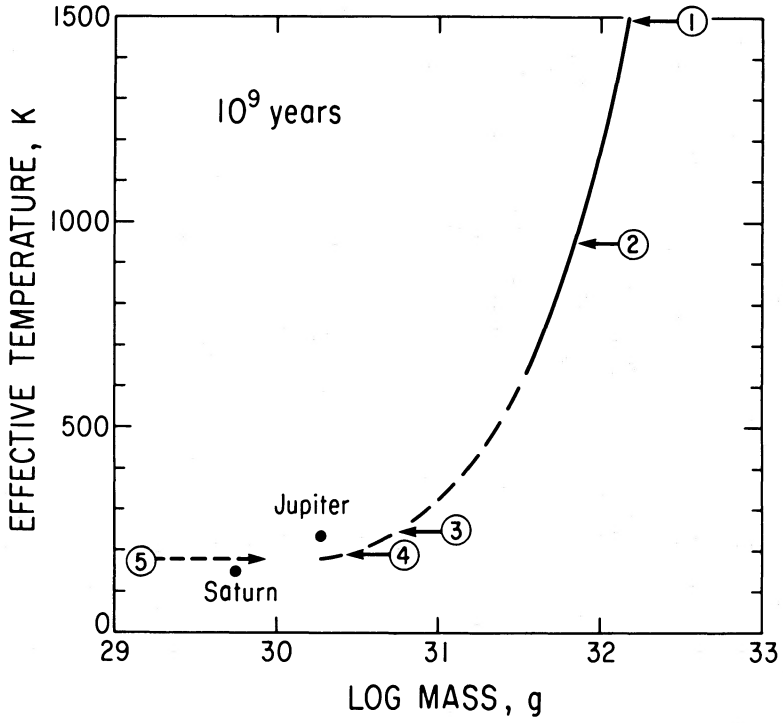

FIG. 19.—Key chemical indicators in evolution of brown dwarfs. Effective temperature as a function of mass is plotted for brown dwarfs at 10^9 yr old (one representative curve only is shown). Points indicate approximate locations of Jupiter and Saturn at this age. Arrows refer to (1) condensation of silicates at 1 bar level, (2) conversion from carbon monoxide to methane as predominant carbon species in atmosphere, (3) condensation of water clouds at 1 bar pressure level, (4) conversion from molecular nitrogen to ammonia as predominant nitrogen species in atmosphere, (5) rainout of helium in interior. All arrow locations are approximate.

TABLE 4

RELEVANT OBSERVATIONAL TECHNIQUES

Technique/facility	Capability	Requirements
Earth-based near- to mid-infrared speckle interferometry	Detection, luminosity, atmosphere composition (C/O, grain composition), time variability	Technique exists; require broad-band spectra 1–10 μm
IRAS, far-infrared	Detection, atmosphere composition, dust properties in atmosphere	Data now exist; systematic search
HST 1st generation instruments	Visible and ultraviolet detection, orbit determination, variability	Systematic visible search to identify systems
HST 2nd generation instruments	Near-infrared detection of systems; luminosity, atmosphere composition; orbit; mass (by concurrent astrometry)	Very high spatial resolution and coronography to monitor companions; spectral resolution (R = 500, 0.8–2.5 μm
SIRTF, near- to mid-infrared	Luminosity, atmosphere composition (vertical abundance profiles of gaseous and particulate absorbers)	High spatial resolution to distinguish companion; high spectral resolution to derive vertical abundance profiles

VIII. SUMMARY AND OUTLOOK

We have constructed self-consistent models for the structure, evolution, and observable properties of degenerately cooling objects, or "brown dwarfs." Model atmospheres composed of a range of likely gaseous and particulate opacity sources have been calculated both to provide a boundary condition for interior temperature-pressure profiles and to determine the emergent spectra for such objects. The interior model incorporates our current best understanding of the behavior of hydrogen and helium at very high pressures and provides cooling time scales for objects of varying mass and composition. The radius derived from the interior models is combined with the emergent fluxes calculated from the atmosphere model to fit the MPL data and derive the luminosity and (assuming a rough age) the mass of VB 8B. We find VB 8B to be most probably a 0.05 $M_\odot$ object with effective temperature in the range 1200–1500 K and an atmosphere which very likely contains particulate absorbers. The derived mass is consistent with the limit derived from astrometry. The spectral distribution of emergent flux is also sensitive to the C to O ratio through the presence of water; further modeling must be done to assess precisely the effect of gaseous water and other molecules on the fit to the VB 8B broad-band data. The prospect that significant elemental compositional information regarding these objects may be derived from broad-band data has, however, been established. Finally, key changes in chemical oxidation state and condensation of major constituents during the evolution of brown dwarfs has been presented, and the giant planets of our solar system were placed in context in the evolutionary scheme.

Table 4 lists future observational techniques which could be employed to detect and determine properties of brown dwarfs. Of especial interest are infrared data which could determine the C to O abundance as well as the presence of silicate absorption features near 10 μm wavelength (Lewis and Nye 1979).

We conclude by touching on several theoretical issues on which our study has some bearing. The filling in of the stellar mass function in the brown dwarf range has been well discussed previously (see, e.g., Stevenson 1978). Equally intriguing is the possibility of extending our ideas on how stars and planets form to the intermediate regime of brown dwarfs. Determination of the C to O ratio and existence of refractory condensates in the atmospheres of brown dwarfs, and ultimately the abundance of these constituents relative to hydrogen, will provide a testing ground for such formation models in a mass regime spanning that of planets and stars. In particular, is the metallicity of the companion similar to that of its primary (binary formation), or enhanced (planetary formation)? Models for the formation and evolution of degenerately cooling objects predict envelope compositions enhanced in some heavy elements but depleted in others (cf. Stevenson 1986). The visible atmospheres of brown dwarfs could exhibit variability due to "weather" and "spots" caused by near-surface magnetic fields (D. J. Stevenson, personal communication). The consequent prospect for time variability should be examined, not only in the infrared but also in the visible and ultraviolet portions of the spectrum.

Detection of brown dwarfs provides new impetus to the experimental and theoretical understanding of the properties of hydrogen in the difficult pressure regime (1–100 Mbars) in which metallization occurs and becomes dominant. As is the case for Jupiter and Saturn, progress in understanding the interiors and evolution of these objects depends on knowing both the behavior of hydrogen itself and the solubility of heavier constituents in hydrogen. Understanding physical processes manifested in the properties and formation of the continuum of objects ranging from planetary to stellar masses is a primary challenge provided by the observation of brown dwarfs.

We thank J. Lewis for the use of his program to calculate the equilibrium abundances of molecular species; D. McCarthy, Jr., R. Probst, F. Low, D. Crisp, D. Hunten, J. Lewis, L. Lebofsky, G. Sill, D. Stevenson, and H. Van Horn for helpful discussions; and D. Stevenson for his review of the manuscript. This work was supported by NASA grant NAGW-192.

REFERENCES

Abramowitz, M., and Stegun, I. A. 1968, *Handbook of Mathematical Functions* (Washington: US Government Printing Office).
Alexander, D. R. 1986, *Ap. J.*, submitted.
Alexander, D. R., Johnson, H. R., and Rypma, R. L. 1983, *Ap. J.*, **272**, 773.
Anders, E., and Ebihara, M. 1982, *Geochim. et Cosmochim.*, **46**, 2263.
Aumann, H. H., *et al.* 1984, *Ap. J. (Letters)*, **278**, L23.
Bahcall, J. N. 1984, *Ap. J.*, **276**, 169.
Barshay, S. S., and Lewis, J. S. 1976, *Ann. Rev. Astr. Ap.*, **14**, 81.
Birnbaum, G., and Cohen, E. R. 1976, *Canadian J. Phys.*, **54**, 593.
Bjoraker, G. 1985, Ph.D. thesis, University of Arizona, Tucson.
Cameron, A. G. W. 1978, in *Protostars and Planets*, ed. T. Gehrels (Tucson: University of Arizona Press), p. 453.
Chandrasekhar, S. 1960, *Radiative Transfer* (New York: Dover).
Clayton, D. D. 1968, *Principles of Stellar Evolution and Nucleosynthesis* (New York: McGraw-Hill).
Conrath, B. J., Gautier, D., Hanel, R. A., and Hornstein, J. S. 1984, *Ap. J.*, **282**, 807.
Conrath, B. J., and Gierasch, P. J. 1983, *Nature*, **306**, 571.

Copeland, H., Jenson, J. O., and Jorgensen, H. E. 1970, *Astr. Ap.*, **5**, 12.
D'Antona, F., and Mazzitelli, I. 1985, *Ap. J.*, **296**, 502.
Edwards, D. K., Glassen, L. K., Hauser, W. C., and Tuchscher, J. S. 1967, *Trans. Am. Soc. Mech. Engr. J. Heat Transfer*, **89**, 219.
Gingerich, O. 1964, in *Proc. 1st Harvard-Smithsonian Conf. on Stellar Atmospheres* (SAO Spec. Rept., No. 167), p. 17.
Graboske, H. C., Jr., and Grossman, A. S. 1971, *Ap. J.*, **170**, 363.
Graboske, H. C., Jr., Pollack, J. B., Grossman, A. S., and Olness, R. J. 1975, *Ap. J.*, **199**, 265.
Grossman, A. S., and Graboske, H. C., Jr. 1973, *Ap. J.*, **180**, 195.
Grossman, A. S., Graboske, H. C., Jr., Pollack, J., Reynolds, R., and Summers, A. 1972, *Phys. Earth Planet. Interiors*, **6**, 91.
Grossman, A. S., Hays, D., and Graboske, H. C., Jr. 1974, *Astr. Ap.*, **30**, 95.
Harrington, R. S. 1986, in *Astrophysics of Brown Dwarfs*, ed. M. Kafatos (Cambridge: University Press), in press.
Harrington, R. S., Kallarakal, V. V., and Dahn, C. C. 1983, *A.J.*, **88**, 1038.
Hayashi, C., and Nakano, Y. 1963, *Progr. Theor. Phys.*, **30**, 460.
Hubbard, W. B. 1973, *Ap. J.* (*Letters*), **182**, L35.
———. 1977, *Icarus*, **30**, 305.
———. 1980, *Rev. Geophys. Space Phys.*, **18**, 1.
———. 1986, *Icarus*, submitted.
Hubbard, W. B., and DeWitt, H. E. 1985, *Ap. J.*, **290**, 388.
Hubbard, W. B., and Lampe, M. 1969, *Ap. J. Suppl.*, **18**, 297.
Hubbard, W. B., and MacFarlane, J. J. 1980, *J. Geophys. Res.*, **85**, 225.
———. 1985, *Ap. J.*, **297**, 133.
Hubbard, W. B., and Smoluchowski, R. 1973, *Space Sci. Rev.*, **14**, 599.
Hubbard, W. B., and Stevenson, D. J. 1984, in *Saturn*, ed. T. Gehrels and M. S. Matthews (Tucson: University of Arizona Press), p. 47.
Hunten, D. M. 1973, *J. Atm. Sci.*, **30**, 726.
Hunten, D. M., Tomasko, M., and Wallace, L. 1980, *Icarus*, **43**, 143.
JANAF Thermochemical Tables, 1971, (NSRDS-NBS 37; Washington: US Government Printing Office).
Johnson, H. R. 1982, *Ap. J.*, **260**, 254.
Lewis, J. S., and Nye, E. P. 1979, *Ap. J.*, **234**, 154.
Linsky, J. L. 1969, *Ap. J.*, **156**, 989.
Lippincott, S. L. 1978, *Space Sci. Rev.*, **22**, 153.
Ludwig, C. B. 1971, *Appl. Optics*, **10**, 1057.
MacFarlane, J. J. 1984, *Ap. J.*, **280**, 339.
MacFarlane, J. J., and Hubbard, W. B. 1983, *Ap. J.*, **272**, 301.
McCarthy, D. W., Jr. 1986, in *Astrophysics of Brown Dwarfs*, ed. M. Kafatos (Cambridge: University Press), in press.
McCarthy, D. W., Jr., Probst, R. G., and Low, F. J. 1985, *Ap. J.* (*Letters*), **290**, L9 (MPL).
Mihalas, D. 1967, *Meth. Comp. Phys.*, **7**, 1.
———. 1968, *Galactic Astronomy* (San Francisco: Freeman).
———. 1978, *Stellar Atmospheres* (San Francisco: Freeman).
Mizuno, H. 1980, *Progr. Theor. Phys.*, **64**, 544.
Nellis, W. J., Ross, M., Mitchell, A. C., Van Thiel, M., Young, D. A., Ree, F. H., and Trainor, R. J. 1983, *Phys. Rev. A*, **27**, 608.
Nelson, L. A., Rappaport, S. A., and Joss, P. C. 1985, *Nature*, **316**, 42.
Patch, R. W. 1971, *J. Quant. Spectrosc. Rad. Transf.*, **11**, 1331.
Pollack, J. B., McKay, C. P., and Christofferson, B. M. 1985, *Icarus*, **64**, 471.
Pollack, J. B., Toon, O. B., and Khare, B. N. 1973, *Icarus*, **19**, 372.
Prinn, R. G., and Olaguer, E. P. 1981, *J. Geophys. Res.*, **86**, 9895.
Probst, R. G. 1977, *A.J.*, **82**, 656.
———. 1983, *Ap. J.*, **274**, 237.
Probst, R. G., and Liebert, J. 1983, *Ap. J.*, **274**, 245.
Reid, N., and Gilmore, G. 1984, *M.N.R.A.S.*, **206**, 19.
Reif, F. 1965, *Fundamentals of Statistical and Thermal Physics* (New York: McGraw-Hill).
Rossow, W. V. 1978, *Icarus*, **36**, 1.
Salpeter, E. E. 1955, *Ap. J.*, **121**, 161.
Stevenson, D. J. 1978, *Proc. Astr. Soc. Australia*, **3**, 227.
———. 1982*a*, *Planet. Space Sci.*, **30**, 755.
———. 1982*b*, *Ann. Rev. Earth Planet. Sci.*, **10**, 257.
———. 1985, *Icarus*, **62**, 4.
———. 1986, in *Astrophysics of Brown Dwarfs*, ed. M. Kafatos (Cambridge: University Press), in press.
Stevenson, D. J., and Salpeter, E. E. 1976, in *Jupiter*, ed. T. Gehrels (Tucson: University of Arizona Press), p. 85.
———. 1977*a*, *Ap. J. Suppl.*, **35**, 221.
———. 1977*b*, *Ap. J. Suppl.*, **35**, 239.
Stone, P. H. 1976, in *Jupiter*, ed. T. Gehrels (Tucson: University of Arizona Press), p. 586.
Tarter, J. C. 1975, Ph.D. thesis, University of California, Berkeley.
Trafton, L. M. 1966, *Ap. J.*, **146**, 558.
Tsuji, T. 1971, *Pub. Astr. Soc. Japan*, **23**, 553.
Van de Hulst, H. C. 1957, *Light Scattering by Small Particles* (New York: Wiley).
Vandenberg, D. A., Hartwick, F. D. A., Dawson, P., and Alexander, D. R. 1983, *Ap. J.*, **266**, 747.
Vardya, M. S. 1965, *Ap. J.*, **129**, 205.
Weast, R. C., ed. 1967, *CRC Handbook of Chemistry and Physics* (Cleveland: Chemical Rubber Co.).
Zapolsky, H. S., and Salpeter, E. E. 1969, *Ap. J.*, **158**, 809.

W. B. HUBBARD, J. I. LUNINE, and M. S. MARLEY: Lunar and Planetary Laboratory, University of Arizona, Tucson, AZ 85721